UCL Université catholique de Louvain

École polytechnique de Louvain (EPL)

Origami folded 2D-crystals

Dissertation presented by
Alice NSENGIMANA

for obtaining the Master's degree in
Chemical and Materials Engineering
Option: Nanotechnology

Supervisors
Benoît HACKENS

Readers
Bernard NYSTEN, Thomas PARDOEN

Academic year 2017-2018

Acknowledgements

The achievement of this master thesis would not have been possible without the help of many people. Working on this project has not just been interesting and academically rewarding, it also has been a real pleasure. So,

...to Andra Iordanescu and Nicolas Moreau for their good humour and comments,

...to Prof. Thomas Pardoen for taking the time to read this thesis,

...to Winfab platform users for their welcoming and support,

...to Prof. Bernard Nysten and Cécile d'Hease for their time, helpful advices and participation,

...to Boris Brun-Barrière, Sébastien Toussaint and Prof. Benoît Hackens for the reachability, investment and patience,

...to my family (and in particularly my dad) for all the encouragement,

Thank you

Alice NSENGIMANA

Louvain-la-Neuve, June 2018

Abstract

Origami folded 2D-crystals

by Alice NSENGIMANA

After the discovery of graphene, 2D crystals raised a huge interest and researches around this area have kept growing ever since. Amongst those 2D materials, hBN stands out. With its structure analogue to graphene and its large band gap, it is a basic building block of complex architectures (heterostructures,...). As any other material, 2D crystals develop defects (vacancies, wrinkles,...) that affect strongly their properties. In hBN deposited on a SiO_2 substrate, wrinkles produced by high-temperature annealing have been reported. They seem oriented in a peculiar way linked somehow to the symmetry of the crystal[1]. For this work, a similar experiment on hBN was performed with BaF_2 as substrate. The topography of the resulting wrinkles was measured by atomic force microscopy and their geometrical parameters were studied as a function of critical experimental parameters. Moreover, electrostatic force microscopy revealed a local polarisation around the wrinkles. Indeed, a particular mechanical-electrical coupling was predicted for such crystal: a gradient of deformation should induce a local polarisation. This properties is known as flexoelectricity and could be exhibited by the wrinkles[2]. A significant difference in the surface potential between the flat and the wrinkled regions of hBN flakes has been detected.

Contents

List of Abbreviations

UCL	**U**niversité **c**atholique de **L**ouvain
EPL	**E**cole **P**olytechnique de **L**ouvain
AFM	**A**tomic **F**orce **M**icroscopy
DFT	**D**ensity **F**unctional **T**heory
EFM	**E**lectrostatic **F**orce **M**icroscopy
FFT	**F**ast **F**ourier **T**ransform
RTA	**R**apid **T**hermal **A**nnealing
SEM	**S**canning **E**lectron **M**icroscopy
SLG	**S**ingle **L**ayer of **G**raphene
hBN	**h**exagonal boron nitride
BaF_2	Barium difluoride
SiO_2	Silicon dioxyde
MoS_2	Molybdenum disulfide

List of Figures

Introduction

Every material contains defects. Their appearance is predicted by the second law of thermodynamics which impose disorder in a material. Besides, some defaults in the production processes also bring their share of flaws to the produced material. Not content with being present, imperfections in the crystal influence strongly the electronic, optical and mechanical properties of solids. Indeed, defects govern features like the ductility of metals or the conductance of semiconductors[3]. Often seen as detrimental, avoiding their presence has been a great and important matter that leads to the production of high quality materials. However, they can play a positive role in the solid and alter its properties in a useful way. For example, the doping of silicon crystal to develop p-n junctions. Regardless of the purpose, being able to control the growth of the defects necessitates a deep understanding of their origins and characteristics.

Defects have been largely studied in bulk material but with the discovery of graphene in 2004 and the resulting interest in two dimensional materials that follows, defects in lower dimensionality raise attention. Indeed, divergences between the theoretical and experimental results change the perspective of graphene: it is now perceived as an real flawed material rather than perfect infinitely large layer with periodicity. Structural defects have also been studied in other materials such as semiconducting transition metal dichalcogenides[4].

The motivation of this work is to analyse and characterise the formation of a special type of defect on 2D crystal: wrinkles. Thanks to atomic and electrostatic force microscopy, several features and functionalities of wrinkles have been parsed. The results are presented in this report as follows: first, a state of the art of the two dimensional crystal, the generation of wrinkles on graphene and hexagonal boron nitrid and the flexoelectricity effect that could be induced by the presence of wrinkles. This will be followed by a presentation of the materials and methods. Finally, the results, their discussion as well as a conclusion will be given.

Chapter 1

State of the art

1.1 Two dimensional crystals

A two dimensional crystal consists in a crystal composed by a single layer of atoms. Considered as thermodynamically unstable at finite temperature, 2D crystal materials were neglected by researchers until the discovery of graphene. Its discovery in 2004, considered as groundbreaking, raises a huge interest in the scientific community.

Since then, several means to synthesize graphene as well as other compounds have been developed. They can be classified into two groups : methods that consist in isolating/extracting layers from a 3D material and growing methods. Amongst those synthesis processes, the mechanical exfoliation method, explained with more details later on in this report, can be found. There are also methods like chemical exfoliation, epitaxial growth on metallic or silicon carbide surfaces,... They can, in general, be applied on other materials[5].

In theory, hundreds of material could be considered as 3D base to get a 2D version of them. However, it is important to take into account different aspects such as: the melting temperature decreasing with the thickness of thin film and the passivation on the surface of most materials which enables them to withstand ambient conditions. As a matter of fact, lots of 2D crystals conceivable in principle do not actually survive due to corrosion, decomposition, segregation,... One needs a 3D material which is highly thermally and chemically stable in order to envisage its 2D counterpart. This is, in general, the case of materials used as lubricant such as graphite (the parent material of graphene), hBN as well as MoS_2. Those have been studied the most. Other examples of 2D materials are display in the figure 1.1[5]

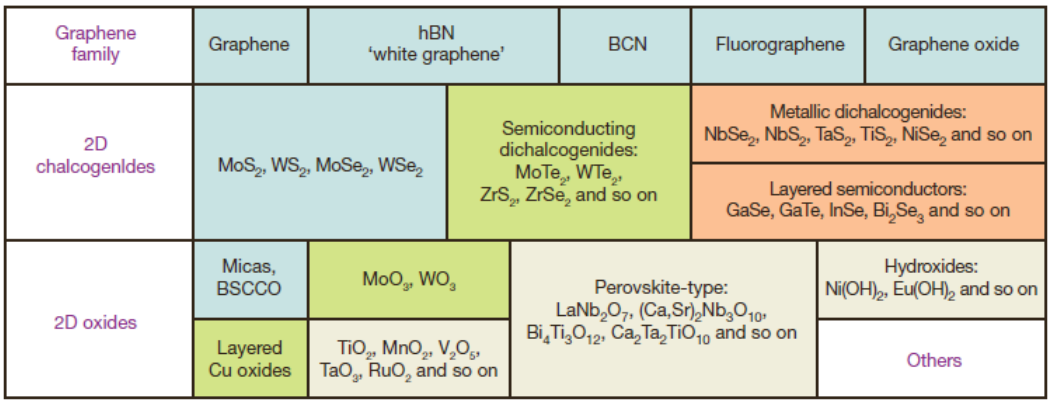

FIGURE 1.1: 2D crystals library. The table is divided in several categories: the stable 2D crystals under ambient conditions are in blue, those that might be stable are in green. Those in pink are instable in air but might be stable in inert atmosphere. Finally in grey, those who have been successfully exfoliated down to the monolayer but for which there is not much information [5].

Thanks to their low dimensionality, 2D crystal materials present unique physical properties. The particularities of their crystal structure could lead to semiconducting behaviour, magnetism or even superconductivity[6]. The potential of those material is tremendous. Indeed, complex architectures such as the one present on figure 1.2 with specific features could be created for specific applications with an approach based on three main steps: synthesis of multiple 2D materials, modification of their chemical, electronic, optical properties by defect engineering, strain engineering or by other ways, and finally assembly of those materials into a 3D structure by, for example, controlled multi-stacking[6]. The variety of eligible materials makes the number of possible structures unlimited however, the acquired properties are more difficult to predict a priori.

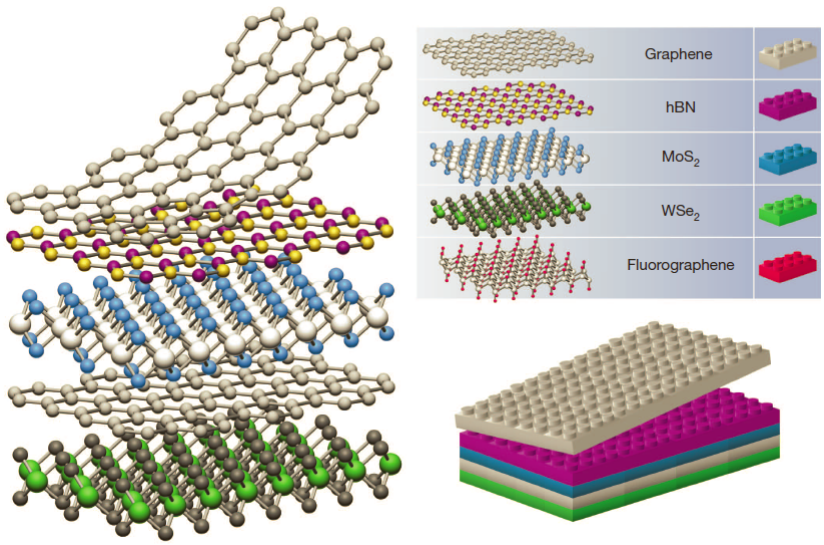

FIGURE 1.2: van Der Waals heterostructure. It can be obtained by stacking of several 2D materials such as hBN, graphene, fluographene,.. [5]

With these unlimited possibilities, plethora of potential applications can be considered, the principal asset being to create materials with the ability to combine several functions (optical, mechanical,...) at once. Some areas could benefit from such a technology like 'smart' ultra-strong nano-composite materials, ultra-fast electronics, solar cells, thin-film transistors,...

1.1.1 Graphite/Graphene

Carbon possesses several crystallographic forms: diamond, graphite and fullerenes. In graphite, carbon atoms bondings involve sp^2 hybridization. This leads to a layered structure with strong covalent interactions within the plane of the layers and with weak van der Waals interactions between the layers. The layers are stacked following an AB sequence (see figure 1.3). A consequence of this structure is the anisotropy of graphite properties. Indeed, graphite is a good electrical and thermal conductor within the layers while way less perpendicular to them[7]. In each layer, the carbon atoms are arranged in a hexagonal pattern. In a graphite unit cell, 4 atoms can be counted. They will be labelled: A, A', B and B'. The atoms A and B stand on a plane while the A' and B' are in the following one. The distance between the two planes in the *c*-axis is 3.35 Å. The difference between the atoms A and B (as well as A' and B') is that the atom A (and A' also) has neighbouring atoms above and below in adjoining planes which is not the case of the atom B (and B') as it can be seen on figure 1.3[7].

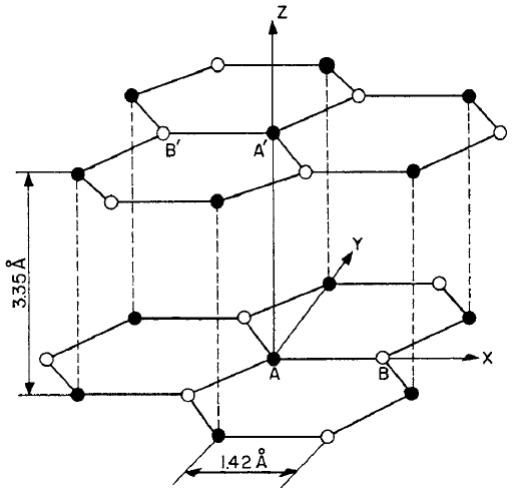

FIGURE 1.3: Graphite crystal structure. The primitive unit cell is hexagonal: $a = 2.46$ Å and $c = 6.71$ Å. There are 4 atoms in the unit cell: A and A′ in black and B and B′ in white [7].

Graphene is the name used to depict one layer of carbon atom with a sp^2 hybridization. Thanks to this configuration, graphene expresses extraordinary properties whether these are mechanical, electrical or thermal. Among them, ambipolar field effect, quantum Hall effect at room temperature, exceptionally high mobility of the carriers as well as sensitivity to single molecule adsorption events have been observed [8]. Indeed, intrisic graphene is defined as a semi-metal or zero-gap semiconductor. A high carrier mobility of the charge carriers at room temperature ($15\,000\,\mathrm{cm^2\,V^{-1}\,s^{-1}}$) has been shown by electrical characterisation. The corresponding resistivity has a value ($1 \times 10^{-6}\,\Omega\,\mathrm{cm^{-1}}$) lower than that of silver (known as the material with the lowest resistivity). Besides, the Johnson noise, generated by thermal agitation of the charge carriers, is low in graphene[9].

The electronic structure of a single layer of graphene (SLG) is unique as it can be seen on the figure 1.4. The charge carriers in this structure with two conical points (K and K′) in the Brillouin zone are described as massless Dirac fermions. At rest, the electrons (and holes) lose their mass and are described by the Dirac equation instead of the Schrödinger equation.

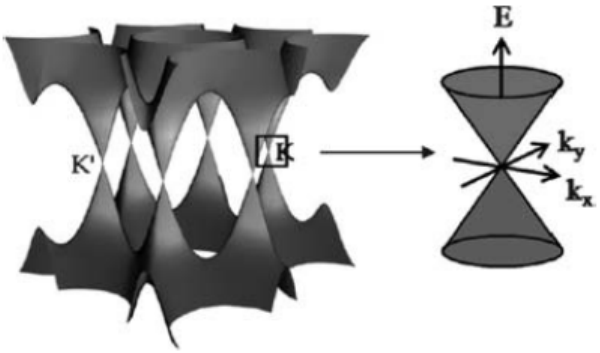

FIGURE 1.4: Electronic band structure of a single layer of graphene[10]

As a result, SLG presents several particular effects such as room-temperature ambipolar field effect, quantum Hall effect or Klein tunnelling effect. In the former, charge carriers can go from hole to electron (and vice-versa) upon changing the gate voltage[9]. The phenomenon is depicted on the figure 1.5. As for the mechanical properties, SLG has been proved to be one of the strongest material with a really high Young's modulus ($\approx 1\,\mathrm{TPa}$)[9].

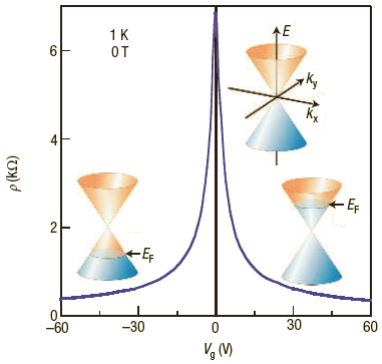

FIGURE 1.5: Ambipolar field effect in single layer of graphene. With 300 nm of SiO_2 layer as substrate and a concentration of charge carriers of $n = \alpha V_g$ with $\alpha \approx 7.2 \times 10^{10}\ \mathrm{cm}^{-2}\ \mathrm{V}^{-1}$ [11]

In bilayer of graphene, the band structure evolves a little compared to SLG. Instead of conical bands, it is a gapless state with parabolic bands that can be found at the K and K' points in the Brillouin zone as shown in figure 1.6. Therefore, charge carriers in bilayer of graphene have a finite mass and the properties of massive Dirac fermions. Quantum Hall effect has also been detected but with some significant differences from the SLG quantum Hall effect[9].

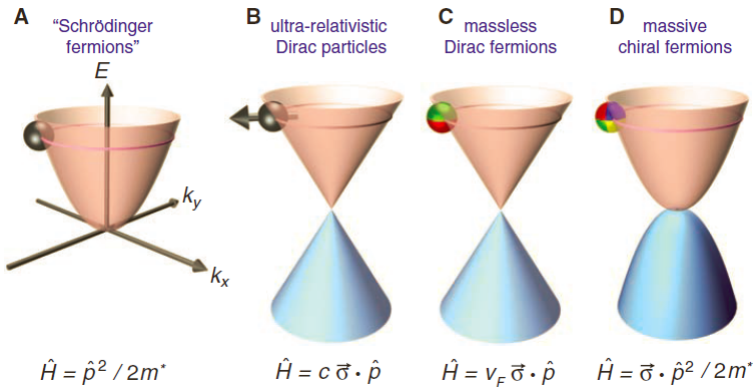

FIGURE 1.6: Electronic band structures. **A** for charge carriers normally described by the Schrödinger equation with an effective mass m^*. **B** for relativistic particles following the Dirac equation with c (the speed of light) and σ (the Pauli matrix). **C** for charge carriers in SLG called massless Dirac fermions with $V_F = 1 \times 10^6\ \mathrm{m\,s}^{-1}$ (the Fermi velocity) and σ (describing two sublattices (red and green) of the honeycomb lattice as a pseudospin matrix). **D** for charge carriers in bilayer of graphene also named massive Dirac fermions. The equation that describes them is a strange combination of features from the Dirac and Schrödinger equations [12].

The applications of graphene are numerous and in several areas like biological engineering, optical electronics, ultrafiltration, composite material and photovoltaic cells [13]. The characteristic stated above make graphene a good sensor. As for the optical properties, since graphene absorbs little of the white light (2.3%), it can be considered as a good transparent conducting electrode[9].

1.1.2 hexagonal Boron Nitride

Hexagonal boron nitride (hBN) is a well-known compound bearing some structural similarities with graphite as it is showed with the values in the table 1.1. It possesses an equal number of boron and nitrogen atoms. Its structure is composed of strong intralayer σ bonds and weak interlayer van Der Waals forces. Boron nitride has several crystalline forms different

from the hexagonal one: sphalerite boron nitride similar to the cubic diamond and wurzite boron nitride resembling hexagonal diamond[14]. Amongst these allotropes, hBN is the most common stable form.

Properties	hBN	Graphite
Bond length [nm]	0.144	0.142
Bond energy [eV]	4	3.7
Interlayer spacing [nm]	0.333	0.335
Young's modulus [TPa]	0.81-1.3	1.1

TABLE 1.1: Comparison of hBN and graphite properties showing the similarities in the structure[15].

The heteroatom bonding leads hBN to be partially ionic unlike the pure covalent C-C bonds in graphite. Therefore, the electrons are localised near the nitrogen in the σ bonds, while the π bonds present filled p orbitals of the nitrogen and empty ones of the boron. Compared to π electrons in graphite, the electrons are less delocalised. Those dissimilarities explain the differences between the two materials in optical, electronical and chemical properties. Indeed, while graphite is highly conductive, hBN possesses an wide band gap (5.9eV [16]) which makes it electrically insulating. It is thermally conductive as well as chemically inert in a plethora of acids.

Another difference between the graphite and its insulating counterpart is the stacking characteristics. Unlike in graphite (see figure 1.7), an hBN stack is composed of planes of superposed hexagons (AA' stacking). The boron and nitrogen atoms are in succession along the c-axis [14]. This peculiar stacking explains the rare occurrences of hBN monolayer compared to graphene.

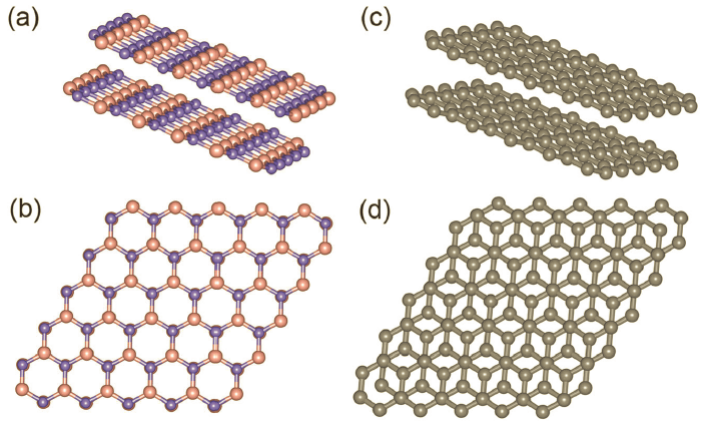

FIGURE 1.7: Comparison of hBN and graphite structures. Structural model of hBN in **a** and **b** as well as the one of graphite in **c** and **d**. Layers of hBN are stacked following an AA' order while graphite follows an AB stacking[14].

Physically, hBN usually consists of a polycristalline solid. It is thermally conductive as well as chemically inert in a plethora of acids. With its particularities, hBN is seen as an attractive compounds in several areas like cosmetics, insulation or lubrication. As a nanomaterial, it is found in deep ultraviolet illuminants, dielectrics gates, insulating thermalconductors, protective coatings,...[15].

As a 2D crystal, hBN is a great substrate for graphene due to its similar bond length and crystal structure as well as protective cover. Indeed, it allows an increase in the electronic quality (such as the mobility) of the latter while protecting it from external conditions. It is also used as gate dielectrics and tunnel barriers [5].

1.2 Wrinkles and origami

Upon uniaxial compression (or extension), most 2D materials shrink (or expand) in the direction of the compressive (or tensile) stress whereas expand (or shrink) in the perpendicular direction. With the decreasing of the thickness scale (towards the micro- or nanoscale), other behaviours may occur such as negative compressibility. With that in mind, one could consider wrinkles as just a typical strain configuration. Nevertheless, physical properties in 2D crystals vary with both the strain and the strain gradient leading for example to the emergence of effects such as "pseudomagnetic" field leading to quantum Hall effect in graphene[17], strain photonic in MoS_2 [18] or, as it will be explained further on in this report, flexoelectricity in hBN[19]. Therefore, wrinkle engineering is an area worth of intensive examination[1].

1.2.1 Formation of wrinkles

The appearance of wrinkles in graphene has been already studied in several theoretical and experimental works. In this section, the focus will be on the formation of wrinkles in a supported graphene under biaxial strain. This can be explained by buckle-induced delamination due to lateral compression on the substrate. The ideas of the following model developed by *Kuan Zhang* and *Marino Arroyo* [20] can be applied to other elastic thin film with weak bonds with the substrates. This is probably the only model in the literature that describes completely the formation of wrinkles in conditions similar to those of the experiments. Besides the description of the wrinkles matches mostly the experimental observations.

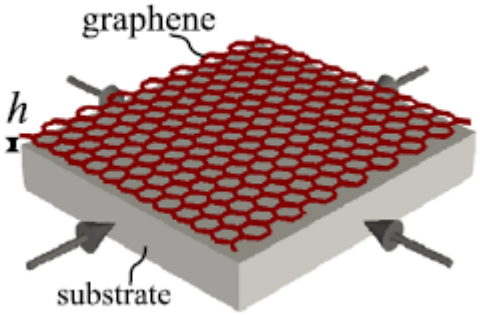

FIGURE 1.8: Setup of the model: graphene flake over a substrate which is laterally compressed. h is the separation between the flake and the substrate[20].

It has been observed that in the case of a uniaxial strain on the substrate, the lateral compression was transmitted to the graphene by frictional forces and led to localised wrinkling (perpendicular to the strain direction)[21]. Theoretically, those wrinkles should be preceded by distributed rippling of smaller amplitude as can be seen on figure 1.9[22]. The observation of a 2D network of wrinkles suggest a biaxial compression[20].

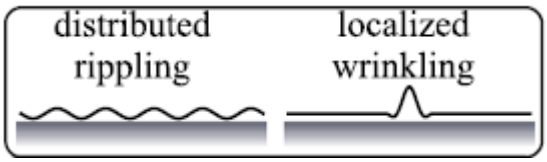

FIGURE 1.9: Out-of-plane deformations: on the left, wave-like disturbance distributed over the sample, known as ripples and on the right, localised out-of-plane deformation with planar vicinity named wrinkle[20].

Numerical modelling

In this model, the domain considered has a surface area of $500 \times 500\ \mathrm{nm}^2$, small enough for the computation and large enough to take into account the wrinkles separation ($\approx 100\,\mathrm{nm}$). The simulations are based on three energetic contributions :

$$U_{el}[\mathbf{x}] + U_{adh}[\mathbf{x}] + U_{fr,k}[\mathbf{x}] \tag{1.1}$$

where $U_{el}[\mathbf{x}]$ is the total elastic energy of the graphene sheet, $U_{adh}[\mathbf{x}]$ and $U_{fr,k}[\mathbf{x}]$ are respectively the total adhesion and friction energies due to the interaction between the graphene and the substrate. The configuration of graphene is described by $\mathbf{x}$ a surface parametrization given by

$$\mathbf{x}(u,v) = (x(u,v), y(u,v), z(u,v)) \tag{1.2}$$

In equation 1.2, $z(u,v)$ represents the coordinate perpendicular to the substrate.

Based on an atomistic-based continuum theory, the first term is expressed as follows:

$$\mathrm{U}_{el}[\mathbf{x}] = \int_{\Omega_0} W(\mathbf{C},\mathbf{K})\mathrm{dS}_0 \tag{1.3}$$

with W the strain energy density which varies with the in-plane strain of the surface $\mathbf{C}$ and its curvature $\mathbf{K}$. S_0 is a reference state without stress and Ω_0 the surface considered.

The interactions between the graphene and the substrate are non-covalent. The results of those interactions are perpendicular adhesive forces with tangential frictional forces in the opposite direction of the sliding. The total adhesion energy is given by

$$U_{adh}[\mathbf{x}] = \int_{\omega_0} \nu(z)\mathrm{dS}_0 \tag{1.4}$$

with ν the adhesion energy density obtained by an effective Lennard-Jones potential between a half-space and a point in graphene. The tangential forces have been modelled as dry friction and have the following form

$$U_{fr,k}[\mathbf{x}] = \int_{\omega_0} \tau_0 K(s_k(u,v))\mathrm{dS}_0 \tag{1.5}$$

where τ_0 is the interfacial shear strength and s_k is the incremental lateral sliding relative to the substrate and $K(t)$ represents a differentiable approximation of $|t|$.

The strain is applied gradually by decreasing the lateral dimensions of the periodic simulation box. This is equivalent to externally deform the substrate. λ_x and λ_y are the stretch ratios, in other words, the proportion between the current and initial dimensions. The compressive areal strain is given by $\epsilon_c = 1 - \lambda_x\lambda_y$. Some assumptions are made:

- the substrate deformation and the externally applied strain are uniformly conformed
- The substrate stays flat.

Spontaneous wrinkling

The appearance of the wrinkles upon isotropic compression involves several steps including a ripples-to-wrinkles transition as it can be seen on the figure 1.10. First, above a given threshold strain, ripples of small-amplitude develop on what was previously at a planar graphene. The ripples are distributed all over the sample according to random orientations. As the compression increases, the deformations localise and merge into short wrinkles, releasing the ripples in their neighbourhood. This occurs due to decohesion of the graphene-substrate

interactions. The height of the wrinkles increases with the compressive strain and the wrinkles create a network that expands. This network splits the sample into different flat domains. In the transition, ripples and some wrinkles disappear, simplifying the network. Indeed, some adjacent wrinkles align and merge[20].

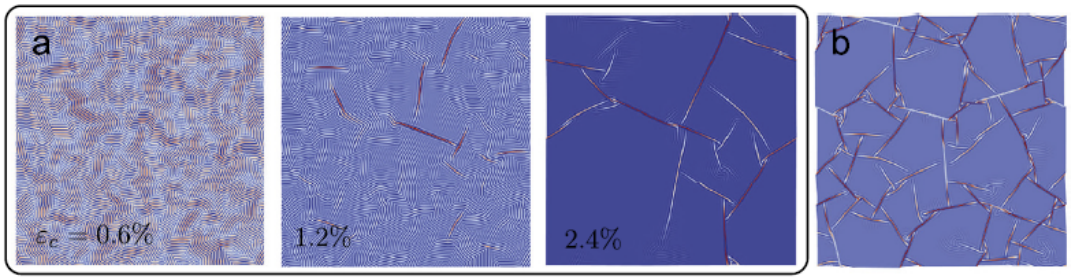

FIGURE 1.10: Scheme of spontaneous wrinkling under biaxial compression. **a** Evolution of the buckling pattern upon isotropic strain ($\tau_0 = 0.3\,\mathrm{MPa}$, $h_0 = 4.5\,\mathrm{nm}$, $\gamma = 0.45\,\mathrm{J\,m^{-2}}$) The blue-to-red map colour gives indication about the out-of-plane displacement. The maximum displacement goes from $2\,\mathrm{nm}$ at $\epsilon_c = 0.6\%$ to $3\,\mathrm{nm}$ at $\epsilon_c = 2.4\%$. **b** Obtained pattern with higher friction $\tau_0 = 1.8\,\mathrm{MPa}$.[20]

Complex geometries can emerge at the junction of the wrinkles but most of them are simple T-junctions. One can note the appearance of Y-junctions as well. The local strain around those junctions is depicted on the figure 1.11. After maturation, the increase of the strain makes the wrinkles grow further without any more organisation[20].

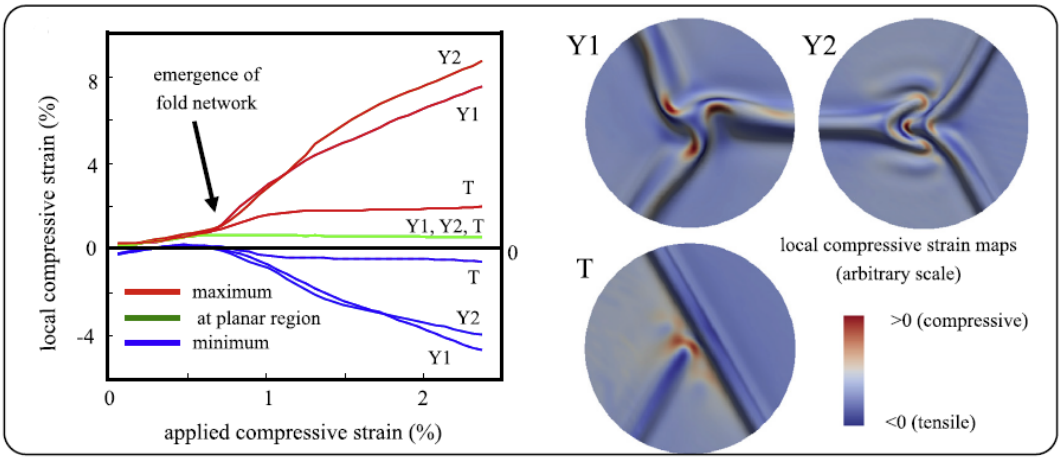

FIGURE 1.11: Local strain behaviour of several types of junctions. The colour map represents the compressive strain and has been adjusted for the different cases: Y1, Y2 and T. [20]

The mechanism of the formation of the wrinkles can be explained by analysing several energy processes as a function of the compressive strain. The figure 1.12 shows those contributions.

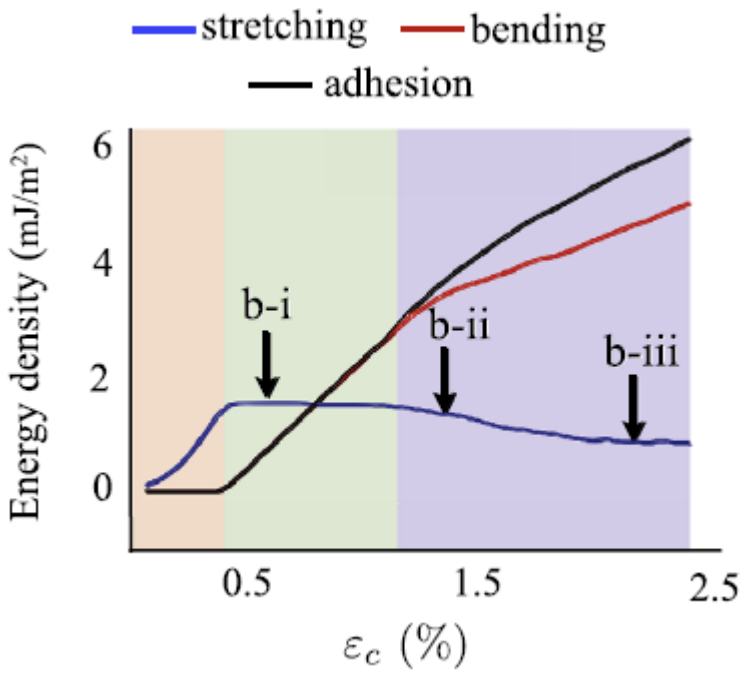

FIGURE 1.12: Energy contributions according to the compressive strain. The red region corresponds to the planar state, the green region depicts the formation of the ripples distributed over the sample and the blue region matches with the formation of the wrinkles. [20]

First (red region on the figure 1.12) the stretching energy is the only contribution as the sample stays planar, at equilibrium distance and evolves quadratically. At a certain threshold (green region on the figure 1.12), as said above, distributed ripples form and bending as well as adhesive contributions participate to the total energy and grow linearly. The stretching energy stays constant. Energetically favourable for the system, the presence of the ripples accommodates the compressive strain. The rippling wavelength is the result of the competition between bending and adhesive energy contributions. For larger strains (blue region on the figure 1.12), it is the presence of the localised wrinkles that relaxes the energy. The bending and adhesive energies increase at a lower rate while the stretching energy decreases gradually.

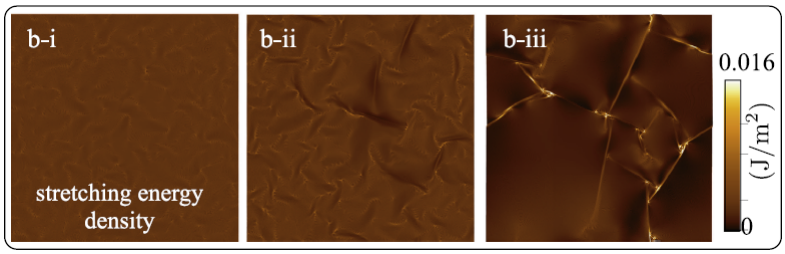

FIGURE 1.13: Stretch energy map for different strain values in the process, as indicated in figure 1.12. [20]

There is a delamination of the graphene from the substrate along the wrinkles. That creates nanochannels where fluids can be trapped. They can produce a certain amount of pressure gradient across the graphene membrane. Evaluating the connectivity and the stability of the network under those conditions is imperative. The figure 1.14 depicts the evolution of the network at the junctions with a fluid introduced in the interstitial space.

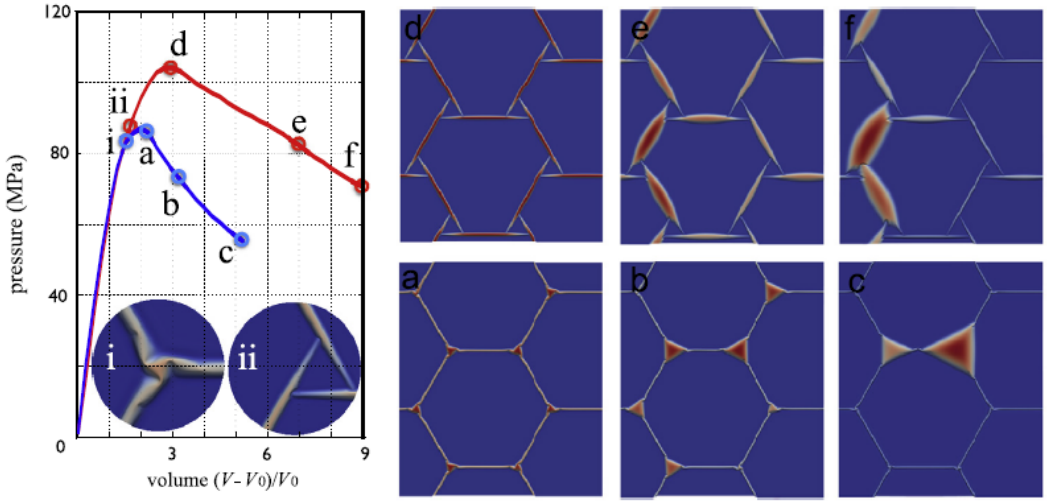

FIGURE 1.14: Stability of the wrinkles under internal pressure due to enclosed fluid. **a-c** represents the evolution of the Y-junctions while **d-f** the T-junction. [20]

1.2.2 Wrinkles in hBN

The formation of wrinkles in a hBN-flakes has been observed in the experimental work of Oliveira *and al.* [1]. Unlike the numerical model, the formation of wrinkles was induced by annealing hBN flakes. Indeed, exfoliated flakes of hBN were transferred onto a Si substrate doped with SiO_2. The flakes were annealed in a quartz tube for $25\,\mathrm{min}$ at $1000\,^{\circ}\mathrm{C}$ with a heating rate of $50\,^{\circ}\mathrm{C\,min^{-1}}$ and a cooling rate of $8\,^{\circ}\mathrm{C\,min^{-1}}$. Figure 1.15-**a** shows the results of a hBN flake after annealing characterised by atomic force microscopy (explained in section 2.3). The flake is only $10\,\mathrm{nm}$ thick. The yellow regions are flat zones divided by wrinkles. On the zoom of a region of the flake (see figure 1.15-**b**), it can be noticed that the pattern obtained is well-defined geometrically. The detailed topography of the wrinkles is shown on the figure 1.15-**c**. The wrinkles on the figure are approximately $40\,\mathrm{nm}$ wide for $10\,\mathrm{nm}$ high. In general, their height goes from $1\,\mathrm{nm}$ to tens of nanometers.

Another divergence with the model presented in subsection 1.2.1 is the orientation of the wrinkles. It can be noticed on the figure 1.15 that the wrinkles are not randomly organised. Some angles are favoured as shown on the fast-Fourier transform (FFT) figure included in the figure 1.15. In general, there are three main orientations and the wrinkles junctions are mostly threefold as on the figure 1.15-**c**. The morphology of a classic junction can be described by connection of the vertices of a small rotated triangle (shaded in red on the figure 1.15-**c**).

Finally, a relation between the orientation of the wrinkles and the crystal lattice has been observed. Apparently, most of the wrinkles occur in the armchair direction.

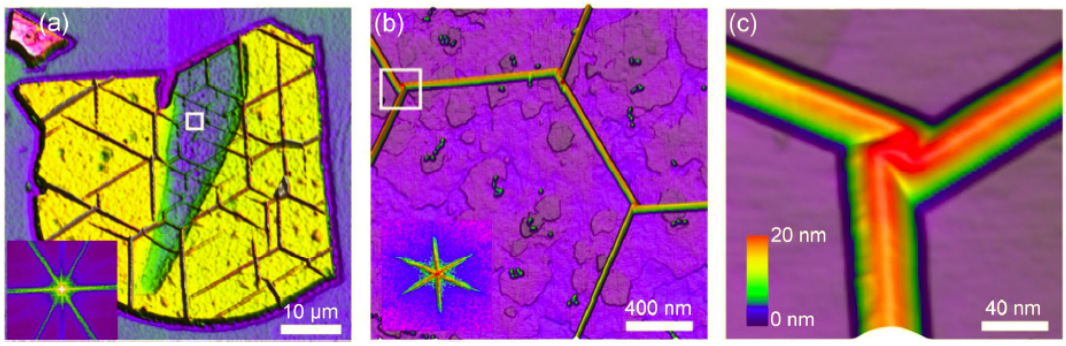

FIGURE 1.15: AFM image of wrinkled hBN-flake after annealing. **a** 10nm thick flake with oriented wrinkles pattern with inset of a FFT. **b** Zoom on a region marked in the **a** image. **c** Zoom on junction marked on **b** image. [1]

The origin of this wrinkling upon annealing treatment could be due to the different and opposite sign in thermal expansion coefficients of the substrate supporting the flakes (Si) and the hBN-flakes. Indeed, Si and hBN along the *c*-axis possess a positive thermal expansion coefficient. However, hBN exhibits an anisotropic behaviour and its thermal expansion coefficient in the plane is negative. As a result, the substrate expands as hBN shrinks during the heating phase while upon cooling, hBN expands and the Si shrinks. As the behaviour of the sample is dominated by the expansion of the substrate, tensile stress is induced within the hBN flakes upon heating and 2D compressive stress during the cooling phase which is responsible for the wrinkling of the flake. The mechanism is similar to the one presented for the graphene, however no crystallographic orientation has been noticed in the case of the graphene and the origin of the compressive stress is due to the difference in thermal expansion coefficients.

The folding pattern of the crystallographic oriented wrinkles junction can be described by the origami formation model, see figure 1.16. In such a model, the unit cells are described by small triangles and the folding that leads to the wrinkles (gray area in the figure 1.16-**a**) can occur along the black lines that form those unit cells. The figures 1.16-**b**,**c** and **d** bring the wrinkles size variety out. The smallest version is shown on figure 1.16-**e**.

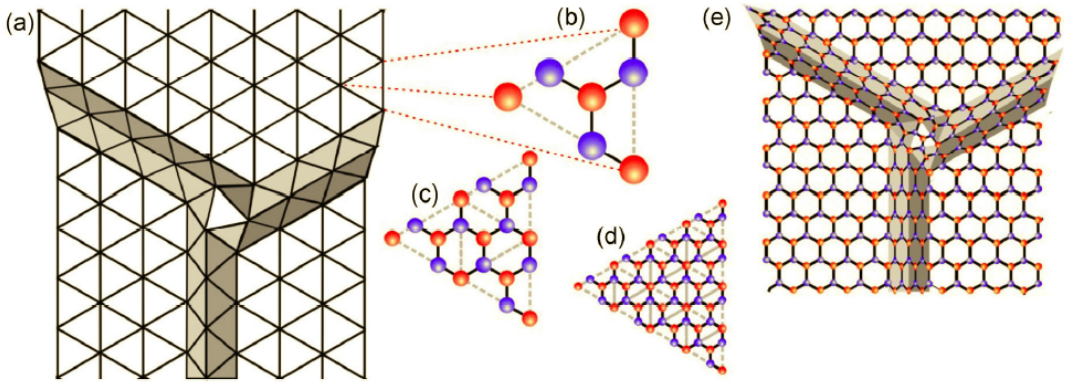

FIGURE 1.16: Origami model for wrinkles junctions. **a** Scheme of the folding. **b**,**c**,**d** present the several triangular unit cells with different size. **e** Model for the smallest wrinkle junction possible [1].

1.3 Flexoelectricity

When one mentions electromechanical properties, one usually thinks about piezoelectricity and electrostriction. Because of the weakness of its effect, in most cases flexoelectricity is usually wrongly omitted. However, with the development of nanoscale technologies and the emergence of studies on 2D crystals, the interest is renewed. Indeed, strain gradient at the nanoscale level are larger and result in strong flexoelectric effects as will be explained later on in this section. Moreover, flexoelectricity is a universal property and is not (unlike piezoelectricity) restricted to noncentrosymmetric materials. This enlarges the possible materials that can be used to evidence this effect[2].

1.3.1 Mechanism

Flexoelectricity can be defined as the coupling between strain gradient and electrical polarisation. Thanks to this property, insulators can be polarised due to an inhomogeneous deformation. Indeed, it is important to insist on the fact that flexoelectricity is not linked to a strain (as the piezoelectricity) but to a strain gradient. To illustrate that fact, let's take a plate made from a centrosymmetric crystal. When a homogeneous deformation is applied to it, no polarisation is detected because centrosymmetry is preserved (see figure 1.17-**a**). On the contrary, under a strain gradient, obtained for example by bending the plate, the centrosymmetry is broken leading to a polarisation (see figure 1.17-**b**). Indeed the top and bottom surfaces are not equivalent anymore[2].

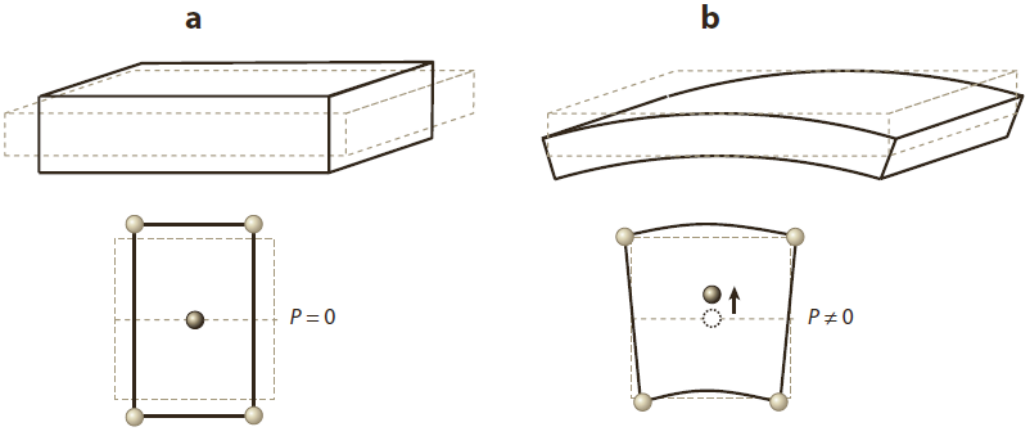

FIGURE 1.17: Flexoelectricity mechanism. **a** Homogeneous strain. **b** Inhomogeneous strain due to bending, for example. In both case, the microscopic mechanism is illustrated beneath[2].

Mathematically, flexoelectricity depends on a fourth-rank tensor which implies that any material of any symmetry could exhibit this effect. Comparatively, piezoelectricity is controlled by a third-rank tensor, hence only noncentrosymmetric materials can be piezoelectric. One could say that in piezoelectric material, the polarisation comes from a low symmetry in the material while flexoelectricity is due to the symmetry-breaking.

At the microscopic level, flexoelectricity could be explained, as on figure 1.17, by the shift of the central cation due to the gradient of strain. This leads to a loss of the centrosymmetry which induces polarisation. Besides, this effect does not just impact the ionic positions but leads also to a redistribution of the electron density which contributes also to the total polarisation[2].

1.3.2 Electronic flexoelectricity

Illustrated in carbon system like graphene, flexoelectricity refers to redistribution of the electron gas in the normal direction upon bending of a 1D or a 2D system due to the increase of the curvature. That yields a local electric dipole in the direction perpendicular to the graphene plane.

For the direct flexoelectric effect, the constitutive equation is

$$P_s = f_D(c_1 + c_2) \tag{1.6}$$

while for the inverse flexoeffect (i.e. deformation is induced by electric field, or polarisation gradient) :

$$c_1 + c_2 = \frac{f_C}{D} E \tag{1.7}$$

In those equations, c_1 and c_2 are the principal curvatures, P_s is the polarisation in $\mathrm{C\,m^{-1}}$, D is the bending stiffness, E the electric field and f_D and f_C are the flexoelectric constants. With the thermodynamic relation from Maxwell, the flexoelectric constants in the previous equations 1.6 and 1.7 have been determined as equal. They are related to the charge distribution of the system[23]. As for the piezoelectricity, the direct flexoelectricity is the appearance of a polarisation due to a strain gradient while the inverse flexoelectricity depicts the appearance of a strain after applying a polarisation gradient[24].

Thanks to DFT calculations, electronic flexoelectricity was modeled in the case of a single graphene sheet. The sheet has been curved into a cylinder with different radii of curvature R and along the zigzag and armchair directions. On the figure 1.18, the evolution of the dipole moment with the curvature is depicted. The dependence is

$$p = \frac{a}{R} \tag{1.8}$$

This relation is valid for large radii of curvature. As the radius decreases, the behaviour varies slightly due to the interaction between the ends of the sheet. This behaviour is supposed to be universal for all low dimensional systems[23].

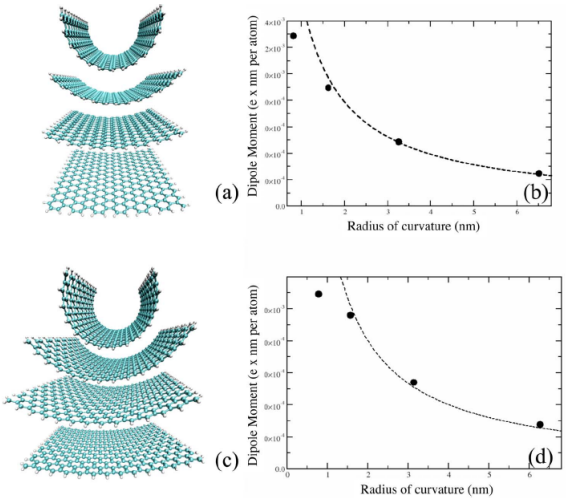

FIGURE 1.18: Flexoelectricity in graphene. **a** an **c** Schema of the bent graphene sheet at different radii of curvature: 0.81, 1.62, 3.24, 6.48 nm along the armchair direction and 0.78, 1.57, 3.13 and 6.26 nm along the zigzag direction[23].

1.3.3 Possible flexoelectricity in hBN

Monolayer hBN possesses symmetry properties that allows it to express effects such as piezoelectricity that its 3D counterpart does not present[25]. The existence of this property leads to potential unusual electromechanical coupling attributes in the few-layers regime. Calculations have shown an uncommon flexoelectric effect in hBN monolayers. Due to an out-of-plane periodic atomic displacements (such as bending of the monolayer sheet), a macroscopic in-plane polarization would be generated. Besides, another contribution to the polarisation is caused by the accompanying deformation stress (which is a typical piezoeffect) [19]. In another work [26], bilayer hBN exhibit a flexoelectric polarization $\approx 10 \times 10^9$ times greater at the same radius of curvature. The application of an in-plane electric field on an anti-parallel bilayer stack will produce favourably a pure shear piezoelectric response in opposite directions for the each layer (see figure 1.19). In the case of the stack being to remain constrained in a planar geometry, the system will exhibit a disappearance of the coherence between the atoms in some region of the bilayers energetically costly. By bending out-of-the original plane, the in-plane strain can be achieved while keeping a coherent stacking at a minimal bending energy cost.

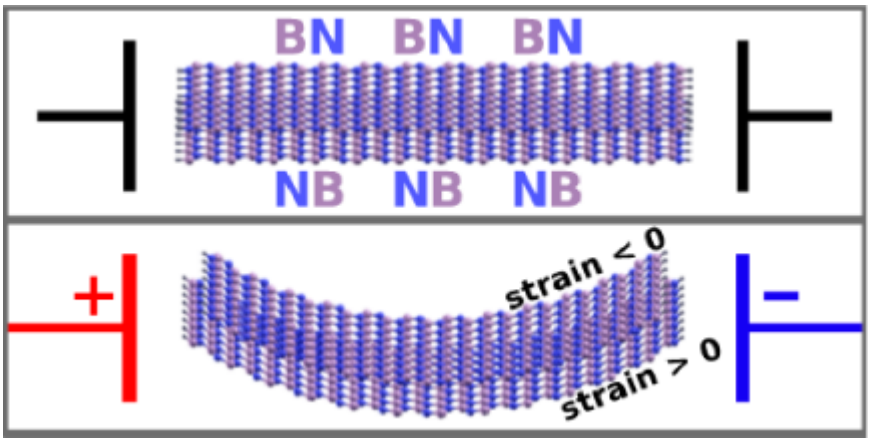

FIGURE 1.19: Mechanical coupling between curvature and electric field in bilayer hBN[26].

That phenomenon appears in only in bilayers as it can be shown on the figure 1.20. Indeed, in the other cases, the introduction of a curvature is not enough to keep the coherence of the stacking[26].

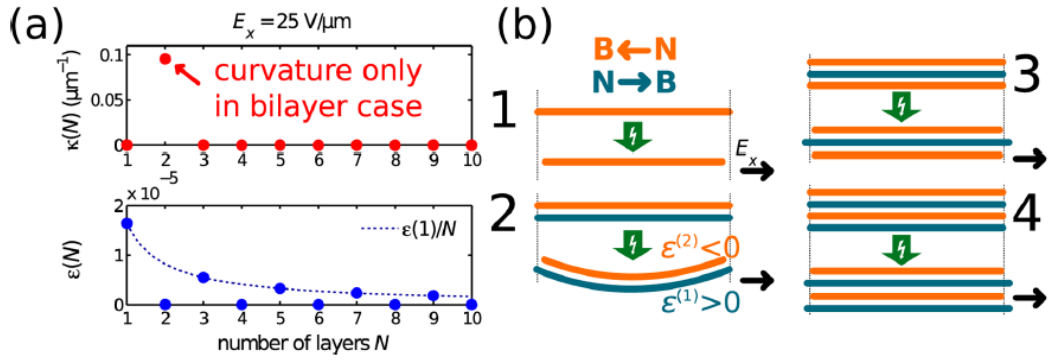

FIGURE 1.20: Curvature κ and average strain ϵ for a stack of N-layers with and electric field of $E_x = 25\ V\ \mu m^{-1}$ on **a**. **b** Presence of a curvature only in the bilayer case[26].

1.4 Objectives

Despite several models concerning wrinkling of 2D crystals, the literature is poor when it comes to experimental data especially regarding wrinkling by thermal treatment. The purpose of this work is to gather as much information as possible about the formation of wrinkles upon annealing in order to validate the mechanical models presented. To do so, flakes of hBN transferred on BaF_2 substrates have been annealed in a RTA furnace. The topography of the flakes after the thermal treatment was characterised by atomic force microscopy.

In addition, the possibility of occurrence of an electric polarisation in the vicinity of the wrinkles will be investigated for the first time in this thesis. To that end, the flakes will be examined by electrostatic force microscopy.

Chapter 2

Materials and methods

2.1 Exfoliation

In order to obtain flakes of hBN, small crystals of the 3D material have been purchased at HQGraphene (see figure 2.1).

FIGURE 2.1: Purchased material: Synthetic hBN [27].

Those crystals have been mechanically exfoliated following the "Scotch Tape" method. In this method, the adhesive tape is used to repeatedly cleave the hBN crystal until a large number of few-layer thick flakes are dispersed on the tape. Thereafter, the tape is gently put into contact with a substrate (BaF_2 or SiO_2) and peeled off, leaving multilayer flakes on the substrate (steps depicted on figure 2.2).

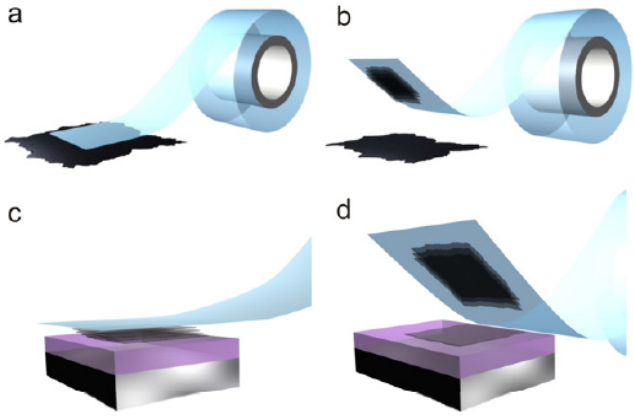

FIGURE 2.2: Exfoliation mechanism: **a** Separation of the crystals into stacks of layers (**b**) with the adhesive tape by repeatedly folding, pressing and unfolding it. The tape gets into contact with the substrate in **c**. It is peeled off in **d** leaving a few layers on the substrate[6].

2.2 Annealing processes

The obtained flakes have been annealed on their substrates in a rapid thermal annealing (RTA) furnace under Ar/H_2 flux. The heating system of the furnace uses an infrared lamp fixed at the focus of the paraboloidal reflector. The infrared beams will be reflected in parallel. Since the lamp is sealed in a quartz glass tube, no gas is generated and the heating is clean. The body of the furnace is made of aluminium and to allow heating to high temperature, the body is cooled with water[28]. A scheme of the furnace assembly is presented on figure2.3.

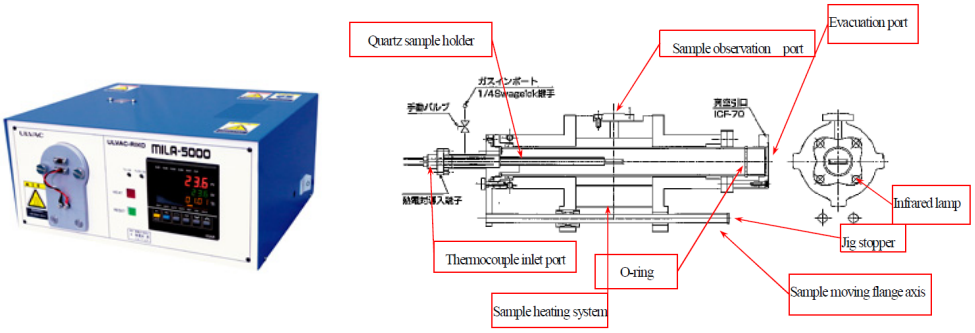

(A) RTA furnace [29]. (B) RTA furnace assembly [28]

FIGURE 2.3: Annealing equipment

The standard thermal process consists in a purge phase of 10 minutes at room temperature. It is followed by the heating phase ($50\,^{\circ}\mathrm{C\,min^{-1}}$) until the furnace reaches $990\,^{\circ}\mathrm{C}$ (this is the maximum temperature that can be reached in this furnace). At this stage, the temperature is held for $10\,\mathrm{min}$ before the cooling phase initiates ($8\,^{\circ}\mathrm{C\,min^{-1}}$ until room temperature) (see figure 2.4) .

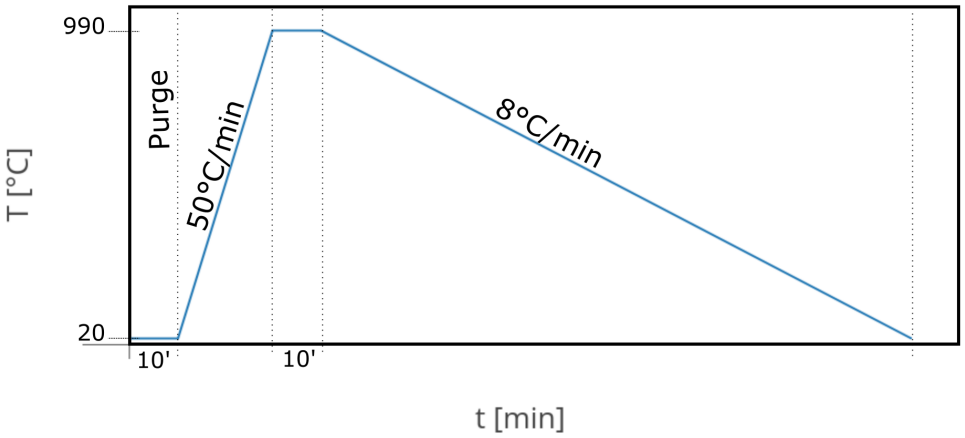

FIGURE 2.4: RTA temperature profile vs time: Standard process

Different processes have been tested. In this report, we will focus on temperature and duration of the high-temperature plateau variations and what changes they will bring in the final structure of the flakes. On the following figures (figures 2.5 and 2.6), several processes variants are depicted.

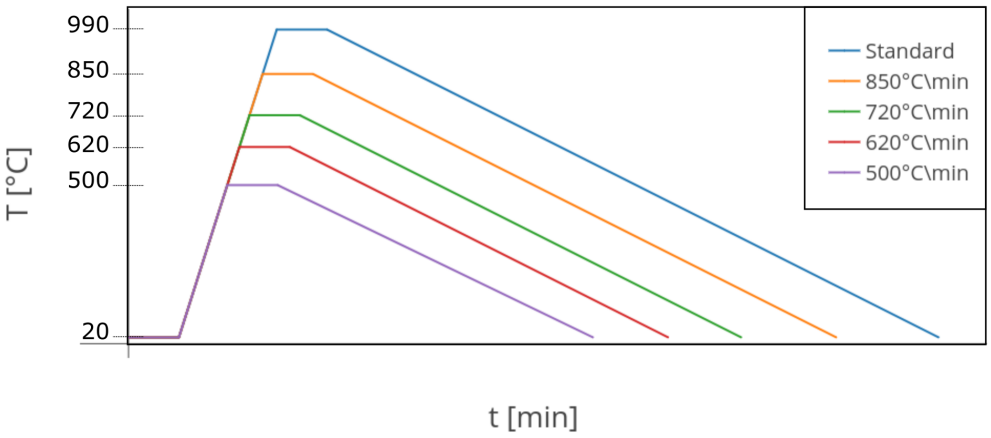

FIGURE 2.5: RTA processes: temperature variation with a 10 step period.

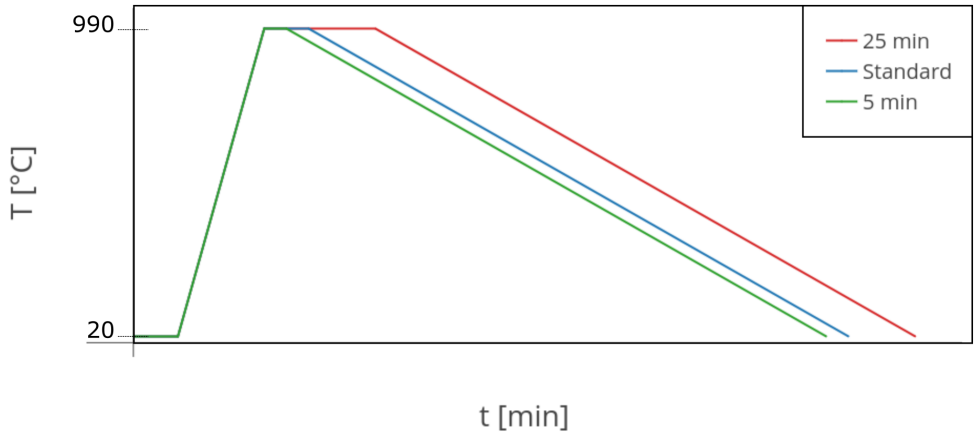

FIGURE 2.6: RTA processes: time variation at 990°C.

2.3 Atomic Force Microscopy

AFM measurements have been performed with an Icon Bruker AFM (see figure 2.7a). The principle of the AFM rests on interactions (attractive and repulsive forces) between a tip assembled on a cantilever and the surface of the sample. The assembly lies on a piezoelectric actuator. During the scanning, the interactions result in motions of the probe that are monitored by a beam deflection measurement system. Indeed, a laser beam is reflected off the back end of the cantilever and onto a sensitive detector. This detector tracks vertical as well as lateral motions of the probe[30]. A feedback mechanism allows the scanner to hold the tip at either a constant force or height above the sample surface. In the first case, the real time height deviation is monitored, while in the second case it is the deflection force on the sample that is recorded[31]. A scheme of the system is shown on the figure 2.7b.

(A) Atomic force microscope: Dimension Icon from Bruker [32].

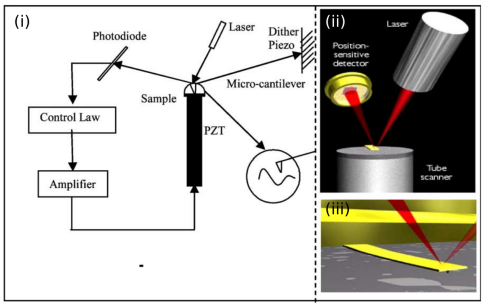

(B) AFM system. **(i)** Scheme of the system.**(ii)** Representation of the system with the detector, the laser, the probe and the sample. **(iii)** Zoom on the probe from **(ii)**[31].

FIGURE 2.7: AFM equipment

Tip-surface Interactions The potential energy V_{ts} between the tip and the sample results in a vertical force between the two: $F_{ts} = -\partial V_{ts}/\partial z$ as well as a tip-sample spring constant: $k_{ts} = -\partial F_{ts}/\partial z$. This force has several contributions which can be classified according to their range and their strength. As can be seen on figure 2.8, it includes chemical short-range forces (red crescents) detected up to a fraction of nanometers and the van Der Waals, the electrostactic and the magnetic forces for which the typical range goes up to $100\,\mathrm{nm}$[33].

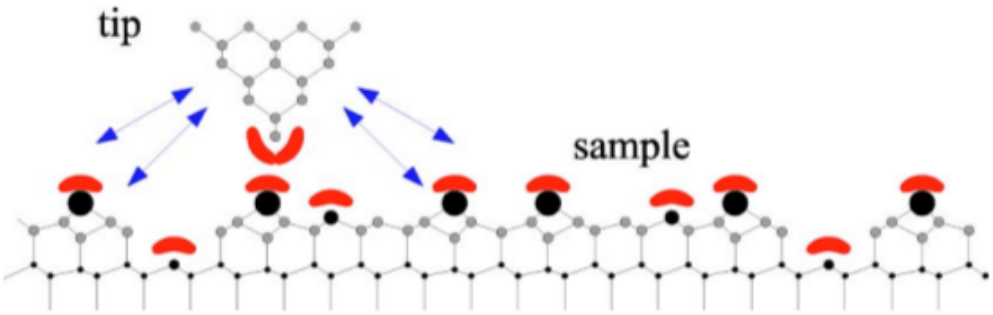

FIGURE 2.8: Force contributions between the tip and the surface sample. The red crescents represent the short-range forces due to chemical interactions while the blue arrows illustrates the long-range forces such as the van Der Waals interactions[33].

The interactions between the tip an the sample vary with the distance between the two. As can be seen on the force-displacement curve on the figure 2.9, when the tip-sample distance is large, weak attractive forces are operating. Those increase as the tip-sample distance decreases up to a point where the tip and the surface become so close that the atoms that compose them start to electrostatically repel each other. This repulsion compensates the attractive forces. At a distance of a couple of Angstroms, the forces are null and becomes strongly repulsive as the distance is further reduced[31].

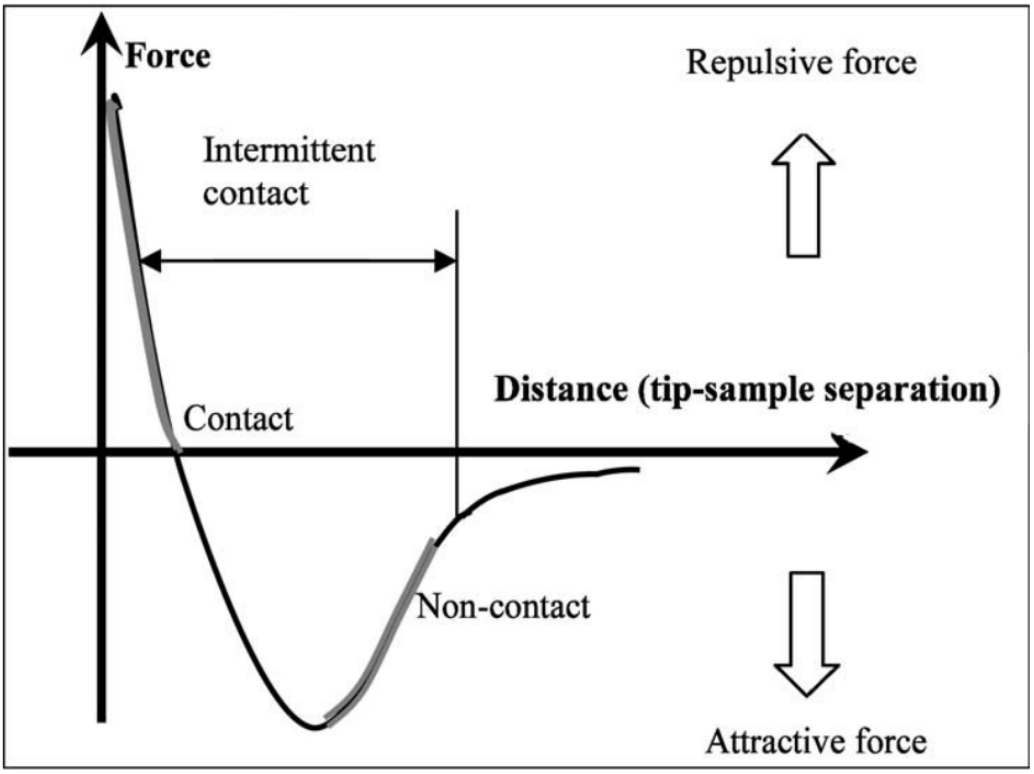

FIGURE 2.9: Force-displacement curve [31]

Open-loop Modes Three main modes are operated with such a system: the non-contact, the contact and the tapping modes (see figure 2.10). On one hand, the non-contact mode allows to extract topographical information by moving the cantilever faintly away from the surface of the sample. The cantilever oscillates at or around its resonance frequency. Shifts from this frequency due to the attraction between the sample and the probe are measured. On the other hand, in the contact mode, the tip of the probe stays in contact with the sample while the interactions between the sample and the probe are monitored. Finally the tapping mode results in a combination of both previous modes. Indeed, the cantilever oscillates at or near its frequency while allowing the tip to touch for a minimal amount of time the surface of the sample [31].

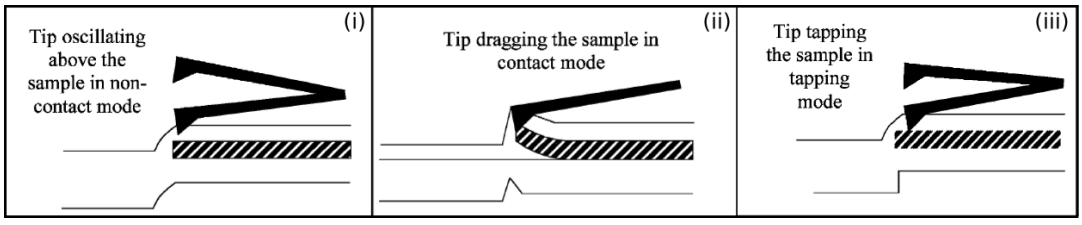

FIGURE 2.10: Open-loop modes. **(i)** Non-contact mode, **(ii)** Contact mode and **(iii)** Tapping mode. Modified from [31].

Tip artefacts Even though AFM is a frequently used method, it has the disadvantage to be (except for non-contact modes) an invasive method. Besides, some images can contain features due to the measurements itself and not present in reality. The presence of those artefacts can be explained by various reasons and can be due to several parts of the microscope. We will focus here on the artefacts due to the shape of the tip (see figures 2.11 and 2.12).Those cannot be avoided and it is important to be aware of their origin and signature[34].

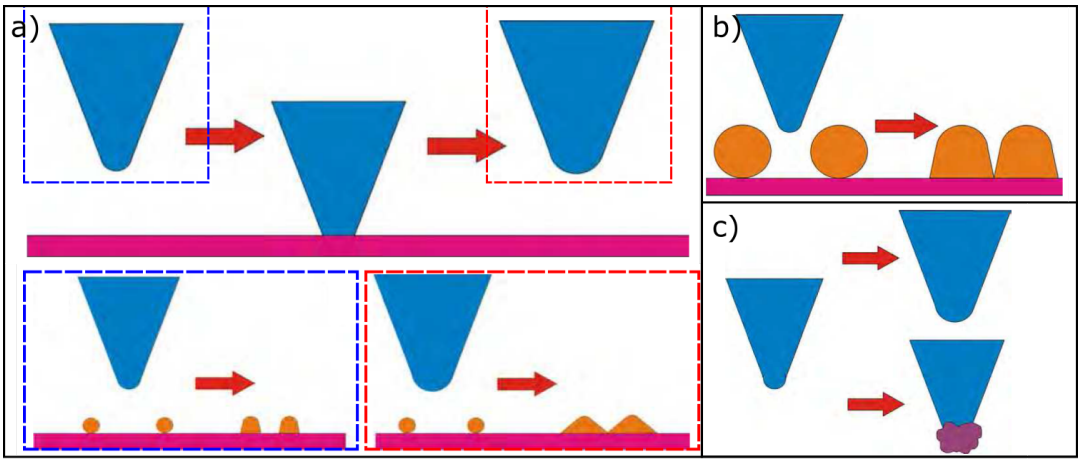

FIGURE 2.11: Tip imaging artefacts. **a** The tip hits the surface of the sample, after that it is possible that it gets blunt. The consequences can be seen below. With a sharper tip, the object is imaged slightly bigger than in reality (left panel, in the blue dashed box). As the tip is wider, the objects appears much bigger than in reality (red dashed box). **b** explains the edge-shape of the object based on the shape of the tip. **c** After a collision with the surface, the tip can get blunt or pick up particles from the surface. It follows a change of the tip mass which alters its resonance frequency. Modified from [34].

The figure 2.11 depicts the convolution effect occurring during the scanning. This appears mostly when the lateral scale of the object to be imaged is similar to the one of the tip. It makes the object look wider than in reality, and conversely, the holes in the surface look narrower. This effect gets worse as the tip widens (see figure 2.11 **a**)[35, 36].

Another artefact due to the tip that could occurs is the double tip/probe effect (see figure 2.12). In this situation, the object is scanned twice by two tips which results in two images: a real one followed by a ghost one. In addition to that, convolution effect can occurs as well.

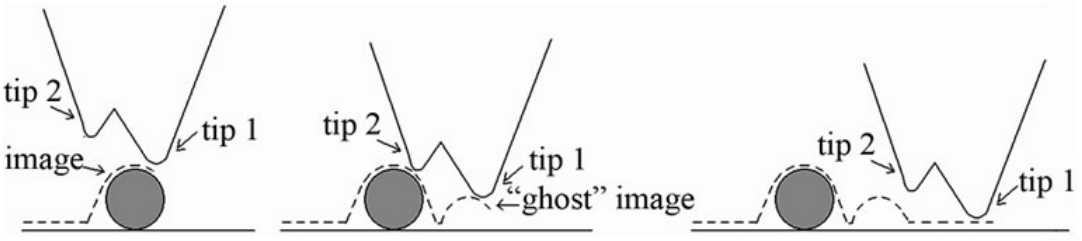

FIGURE 2.12: Double tip effect mechanism [35]

2.3.1 Tapping mode

The topography of the flakes have been extracted by AFM measurements in tapping mode. This method is more attractive than the contact one for several reasons:

- The motion of the tip is sensitive to both forces and force gradients.
- The oscillation amplitude, the frequency, the phase shift and the cantilever deflection can be measured

- Since less contact with the sample is involved, the risk of damaging the tip or the sample is reduced which provides a larger amount of valuable information on the surface.

As briefly explained above, the tapping mechanism consists in driving the cantilever oscillation around its resonance frequency: the image is creating while the feedback alters the distance between the sample and the tip in order to keep the oscillation amplitude constant. The latter can be modified by repulsive forces as well as attractive forces[37].

The cantilever basically behaves like an harmonic oscillator driven by external forces and operating near its resonance frequency:

$$z'' + \gamma z' + \omega_0^2 z = \frac{F_{ex} + F(z)}{m_e} \tag{2.1}$$

z' and z'' represent the derivatives of the distance between the surface and the tip (as a function of time),γ is the damping factor, ω_0 and m_e are respectively the resonance frequency and the mass of the cantilever. Finally, F_{ex} is the external driving force equal to $F_0 \cos \omega t$ while $F(z)$ is the non-linear force probed by the cantilever.

The non linear forces act on the tip on the nanometer scale, so far, away from the surface they are negligible. However, once the probe gets closer, they can be approximated by:

$$F(z) \approx F(z_0) + \frac{\partial F(z_0)}{\partial z}(z - z_0) \tag{2.2}$$

with z_0 the mean distance between the tip and the sample[38, 39].

The probe used for the measurement were specially designed for tapping mode AFM (PPP-NCHR type from NanoSensor). The tip curvature radius is guaranteed to be smaller than $10\,\mathrm{nm}$ while its height is between $10\,\mu\mathrm{m}$ and $15\,\mu\mathrm{m}$[40]. The figure 2.13 depicts the tip under several views while the table 2.1 gives information about the cantilever.

PPP-NCHR		
Property	Nominal value	Specified range
Resonance Frequency [kHz]	330	204-497
Force Constant [$\mathrm{N\,m^{-1}}$]	42	10-130
Thickness [µm]	4	3.0-5.0
Mean Width [µm]	30	22.5-37.5
Length [µm]	125	115-135

TABLE 2.1: Cantilever data[40].

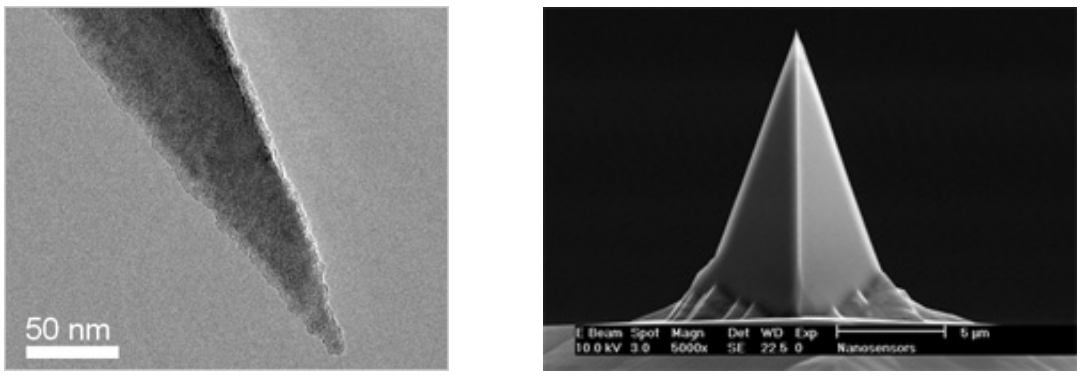

(A) Close up (B) Front view

FIGURE 2.13: SEM images of the tip[40].

2.3.2 Electrostatic force microscopy

The electrostatic force microscopy (EFM) is one of the technique used in non-contact mode. It allows the measurements of electrostatic forces gradient by letting the cantilever oscillating at a certain distance above the sample. The procedure includes two steps (see figure 2.14):

1. **Topography mapping in tapping mode** explained in previous subsection 2.3.1.
2. **Electrical mapping in interleave mode** Just right after the line has been mapped topographically, the probe is lifted and kept at a distance above the sample and the line is scanned a second time. During this second passage, a shift in the phase (or in the frequency) is recorded and a feedback loop is used to maintain the frequency (or the phase) constant. Besides, the tip is electrically biased compared to the sample[38].

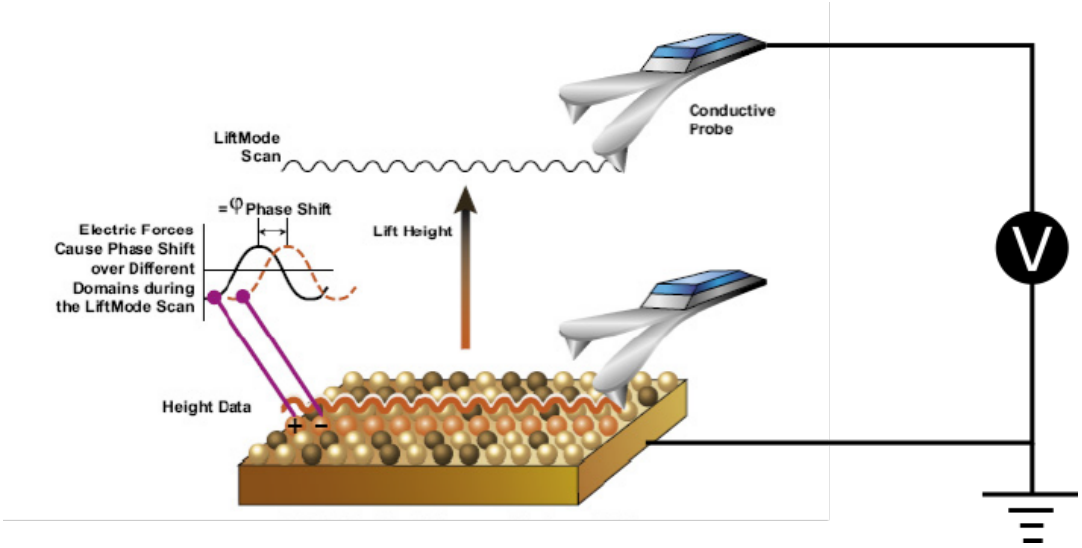

FIGURE 2.14: EFM procedure in double pass [41]

Frequency shifts Frequency shift measurements are directly proportional to the force gradients. Even though phase shifts can be related to frequency shifts thanks to the relation $\Delta\phi/2Q = \Delta\omega/\omega_0$, non-linearity of the phase of the cantilever compared to the frequency makes that relation not valid for large frequencies. Therefore, frequency shift measurements can be seen as more appropriate than phase shift measurements. Based on the equation 2.2, it can be evaluated as follows [39]:

$$\Delta\omega = -\frac{\omega_0}{2k}\frac{\partial F(z_0)}{\partial z} \tag{2.3}$$

Electrostatic force The electrostatic force gradient felt by the tip can be determined by describing the tip-sample system as an ideal capacitance $C(z)$. In case of absence of electric charge in the tip-sample system, we obtain:

$$\frac{\partial F(z_0)}{\partial z} = \frac{1}{2}\frac{\partial^2 C(z)}{\partial z^2}(V_{\text{tip}} - V_{\text{S}})^2 \tag{2.4}$$

with C the capacitance of the tip-sample system, V_{tip} the potential applied on the tip and V_{S} regroups the potential due to the work-function difference between the tip and the surface of the sample as well as other potentials present on the surface. By relating equation 2.4 to the previous equation 2.3, it can be noticed that capacitive forces leads to negative frequency shifts, that vary quadratically with the $(V_{\text{tip}} - V_{\text{S}})$.

Now, if a charge q is introduced in the system, a surface potential proportional to q is generated, we obtain then:

$$\frac{\partial F(z_0)}{\partial z} = \frac{1}{2}\frac{\partial^2 C(z)}{\partial z^2}(V_{\text{tip}} - V_{\text{S}} - V_q)^2 \tag{2.5}$$

$$\frac{\partial F(z_0)}{\partial z} = \frac{1}{2}\frac{\partial^2 C(z)}{\partial z^2}((V_{\text{tip}} - V_{\text{S}})^2 - 2(V_{\text{tip}} - V_{\text{S}})V_q + V_q^2) \tag{2.6}$$

The two additional terms are due to the interactions between the introduced charge q and charges present at the tip apex surface and interaction due to image charge effects. The first additional term is useful since it allows to determine the sign of the charge q while the second one, proportional to q^2 gives negative frequency shifts[39]. The same reasoning goes in case of the introduction of a dipole moment.

It is possible to quantify this charge by scanning a line over the sample including non charged and charged areas at a constant distance. The frequency shift is recorded as the potential of the tip varies. As it can be seen on the figure 2.15, two parabolas are obtained for the charged (green diamond) and the non-charged (red square) areas. This confirms the quadratic relation with respect to V_{tip}. The shift of the minimums of the parabolas is due to the additional potential terms introduced by the charge q[38].

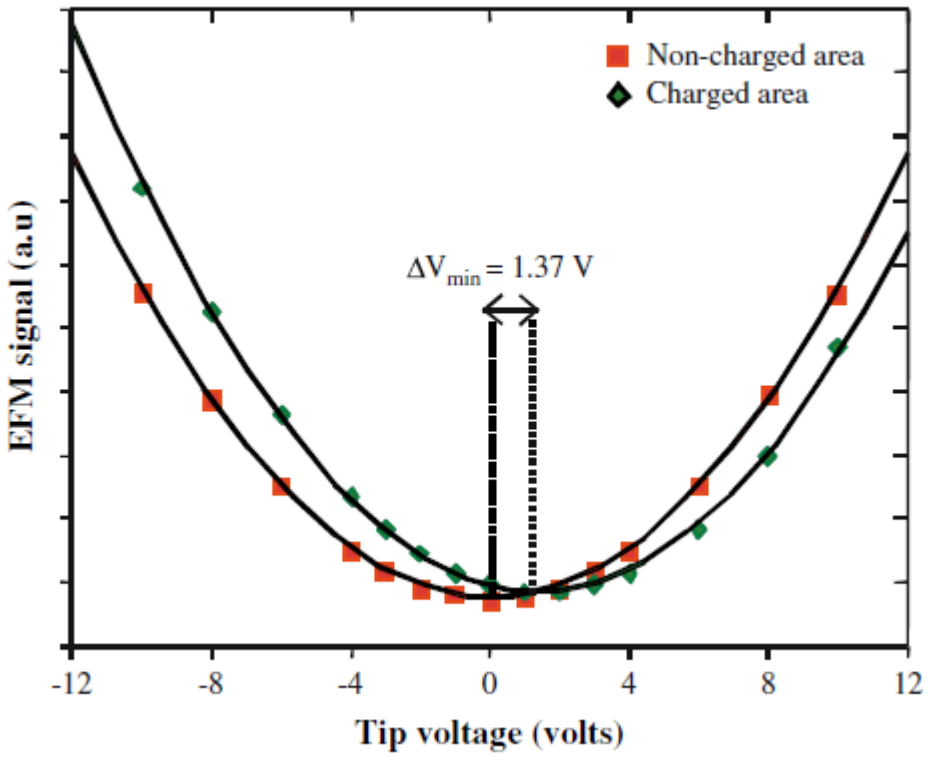

FIGURE 2.15: EFM signal vs tip voltage. The measurement was made at $z_0 = 300\,\text{nm}$ above (non-)charged regions[38].

Capacitive model The force gradient does not only depend on several potentials but also, as the equations 2.4 and 2.6 show it, on the capacitance of the system, more specifically on its second derivative. Therefore, to be able to evaluate it, modelling the tip-substrate system capacitance is necessary.

We can first start by envisaging a simple system where the tip would be a metallic cylinder scanning a sample at a distance z [41] as on the figure 2.16. The cantilever will be ignored

since its contribution is negligible[42].

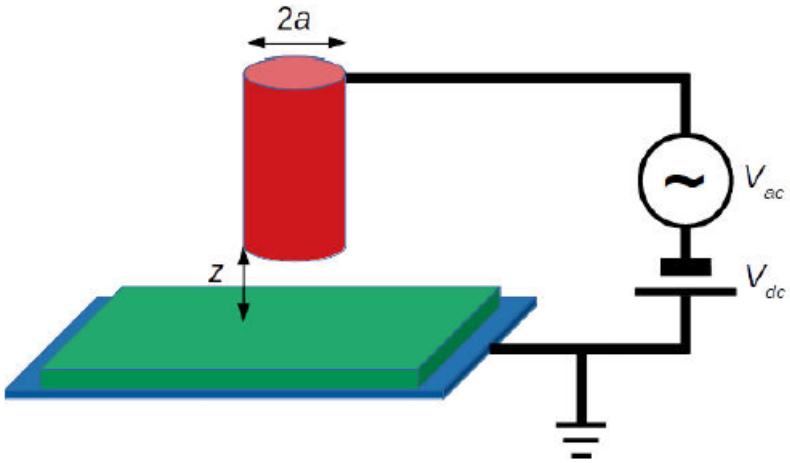

FIGURE 2.16: Simplified capacitance model. The tip is represented by the red cylinder while the substrate is the green parallelepiped.

In this configuration, the capacitance can be expressed by:

$$C(z) = \epsilon \frac{A}{z} \tag{2.7}$$

with ϵ the permittivity of the medium and $A = \pi a^2$ the area of the plane of the surface of the red cylinder end. From it, we can get the second derivative

$$\frac{\partial^2 C(z)}{\partial z^2} = 2\epsilon \frac{A}{z^3} \tag{2.8}$$

Hence, with the relations 2.4 and 2.6, we obtain

$$\frac{\partial F(z_0)}{\partial z} = \frac{\epsilon}{2} \frac{A}{z^3} (V_{\text{tip}} - V_{\text{S}})^2 \tag{2.9}$$

or in case of a charge q

$$\frac{\partial F(z_0)}{\partial z} = \frac{\epsilon}{2} \frac{A}{z^3} ((V_{\text{tip}} - V_{\text{S}})^2 - 2(V_{\text{tip}} - V_{\text{S}})V_q + V_q^2) \tag{2.10}$$

As an expression of the frequency shift, we have with the equation 2.3

$$\Delta\omega = -\frac{\omega_0}{2k} \frac{\epsilon}{2} \frac{A}{z^3} (V_{\text{tip}} - V_{\text{S}})^2 \tag{2.11}$$

or in case of a charge q

$$\Delta\omega = -\frac{\omega_0}{2k} \frac{\epsilon}{2} \frac{A}{z^3} ((V_{\text{tip}} - V_{\text{S}})^2 - 2(V_{\text{tip}} - V_{\text{S}})V_q + V_q^2) \tag{2.12}$$

Other capacitive models can be considered, in particular concerning the aspect of the tip. Another example will be to consider the tip as a truncated cone as on the figure 2.17. The expression for the capacitance second derivative becomes

$$\frac{\partial^2 C(z)}{\partial z} = 2\pi\epsilon[\frac{R^2(^+R)}{z^2(z+R)^2} + K^2(\frac{1}{z+R} + \frac{R}{\sin\theta(z+R)^2})] \quad \text{with K a constant} \tag{2.13}$$

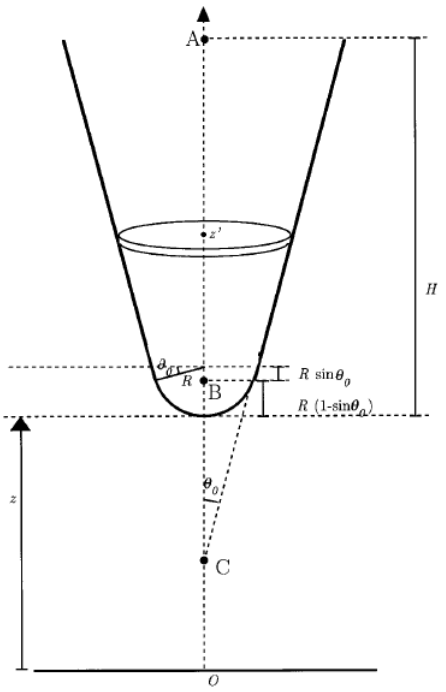

FIGURE 2.17: Characteristic dimension of the tip[42]

The probe used for the measurement were specially designed for EFM (PPP-EFM type from NanoSensor). The tip curvature radius is around $25\,\mathrm{nm}$ while is height is between $10\,\mu\mathrm{m}$ and $15\,\mu\mathrm{m}$[43]. Besides, it is coated with an alloy of $PtIr_5$ to ensure metallic conductivity. The figure 2.18 depicts the tip under several views while the table 2.2 gives information about the cantilever.

PPP-EFM		
Property	Nominal value	Specified range
Resonance Frequency [kHz]	75	45-115
Force Constant [$\mathrm{N\,m^{-1}}$]	2.8	0.5-9.5
Thickness [$\mu\mathrm{m}$]	3	2.0-4.0
Mean Width [$\mu\mathrm{m}$]	28	20-35
Length [$\mu\mathrm{m}$]	225	215-235

TABLE 2.2: Cantilever data[43].

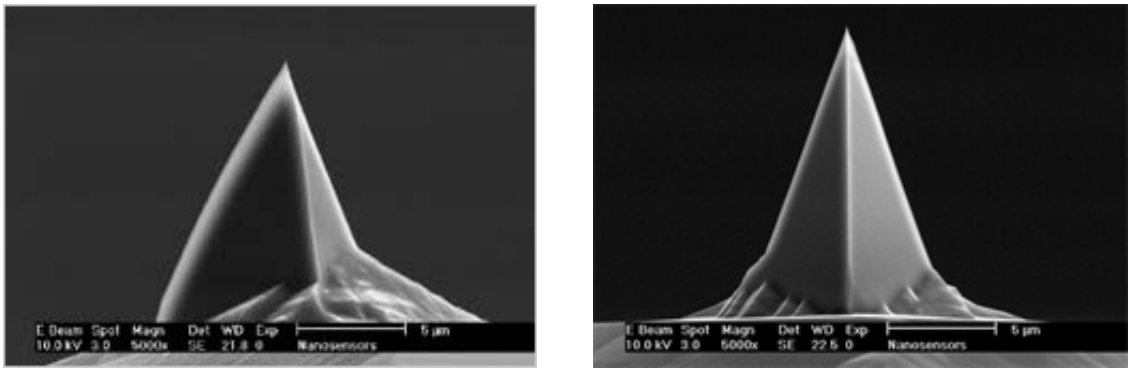

(A) Side view (B) Front view

FIGURE 2.18: SEM images of the tip[43].

Chapter 3

Experimental results

3.1 Topographical characteristics

In the aftermath of the exfoliation step (described in the section 2.1), several flakes are obtained on the substrate. A large amount of diversified shapes, thicknesses and sizes can be observed on one substrate as can be seen on the figure 3.1. A variety of colours is also noticed. Those enable to give a relatively good approximation of the thickness of the flakes.

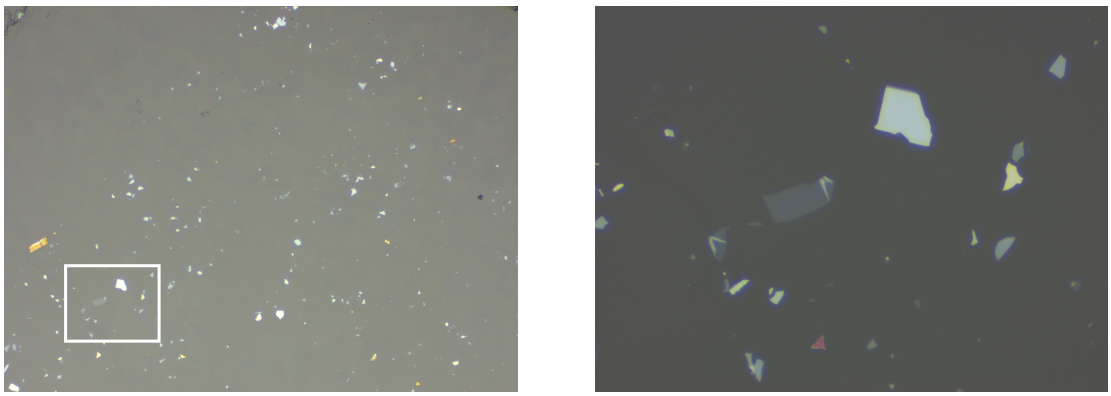

(A) (B)

FIGURE 3.1: Optical microscope images: **A** hBN flakes on BaF_2 substrate (x10). **B** Zoom on the white framed zone in **A** (x50).

Once the exfoliation step is done, the flakes are annealed in a thermal furnace as explained in the section 2.2. The results of the annealing step on the flake can be seen on the figure 3.2. We observe a wrinkled network on the flake where the wrinkles seem to be oriented according to some specific angles. We notice also an iridescence effect at some places as the flake is illuminated. The dark field filter used on the optical microscope allows us to emphasise the wrinkles. We see that they could be separated into subnetworks.

3.1.1 Morphological characteristics

Angles between the wrinkles As stated above, the orientation of the wrinkles does not seem random. After mapping the flake by AFM measurement (in tapping mode) and applying a fast fourier transform (FFT) on the obtained map (see figure 3.3), it can be seen that there is a $60°$ angle between the wrinkles. The FFT also depicts subnetworks of wrinkles slightly shifted compared to each other even though the $60°$ angle between the wrinkles of a same subnetwork is still present. We can also notice the difference in intensity thanks to the colour scale.

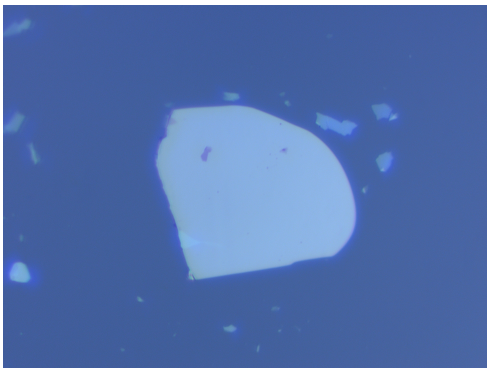

(A)

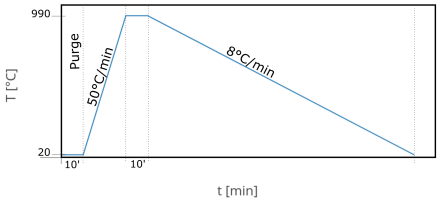

(B)

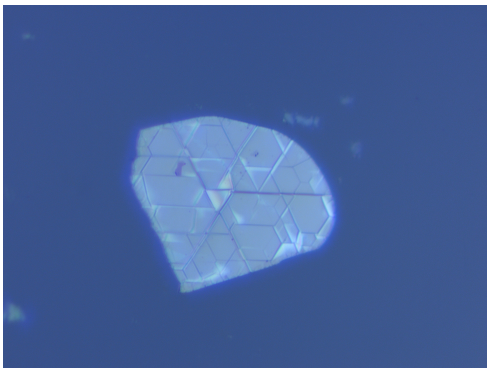

(C)

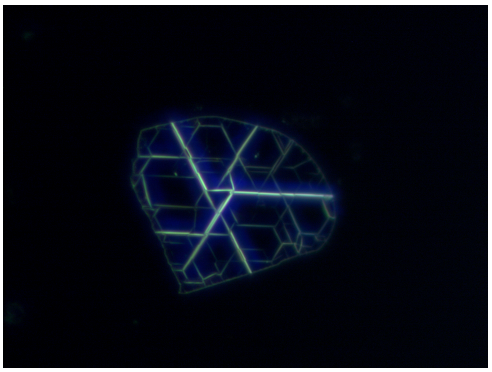

(D)

FIGURE 3.2: Optical microscope images (x100): **A** hBN flake on BaF_2 substrate after exfoliation. **B** Thermal process applied on the flake. **C** Same flake as on figure **A** but after annealing process. **D** Same flake as **A** and **C** under DarkField filter.

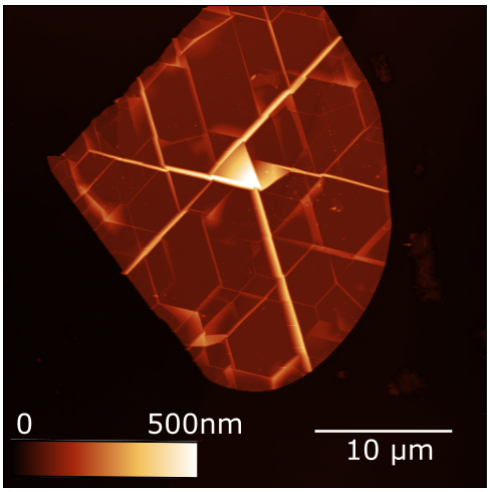

(A)

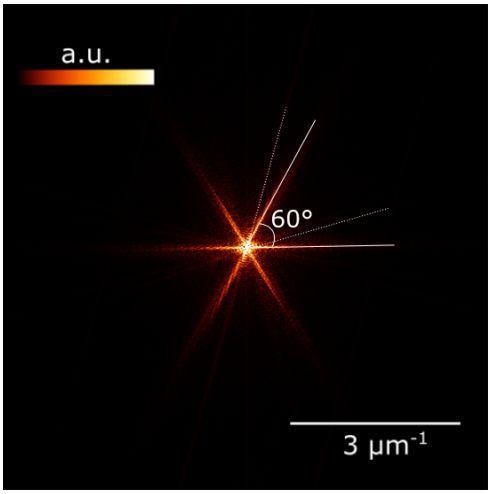

(B)

FIGURE 3.3: Microscope images: **A** AFM topography map of an hBN flake on BaF_2 substrate (same as in figure 3.2. **B** FFT of the AFM topography map on figure **A**

Wrinkles geometry On the figure 3.4, the profile of several wrinkles are depicted. We decided, for the rest of the report, to present the data in the way shown by the dotted frame (that is, subfigures **a** and **b** side by side) for sake of convenience. However, we are aware that this choice might be misleading. This can be illustrated by comparing figure 3.4-**b** and **c**: the latter displays the wrinkle profile with the same scale on the horizontal and vertical axis, i.e. it is much better view of the actual geometry of the wrinkles, while figure 3.4-**c** leads to think

that the wrinkles are sharper than they actually are, due to the aspect ratio of the graph.

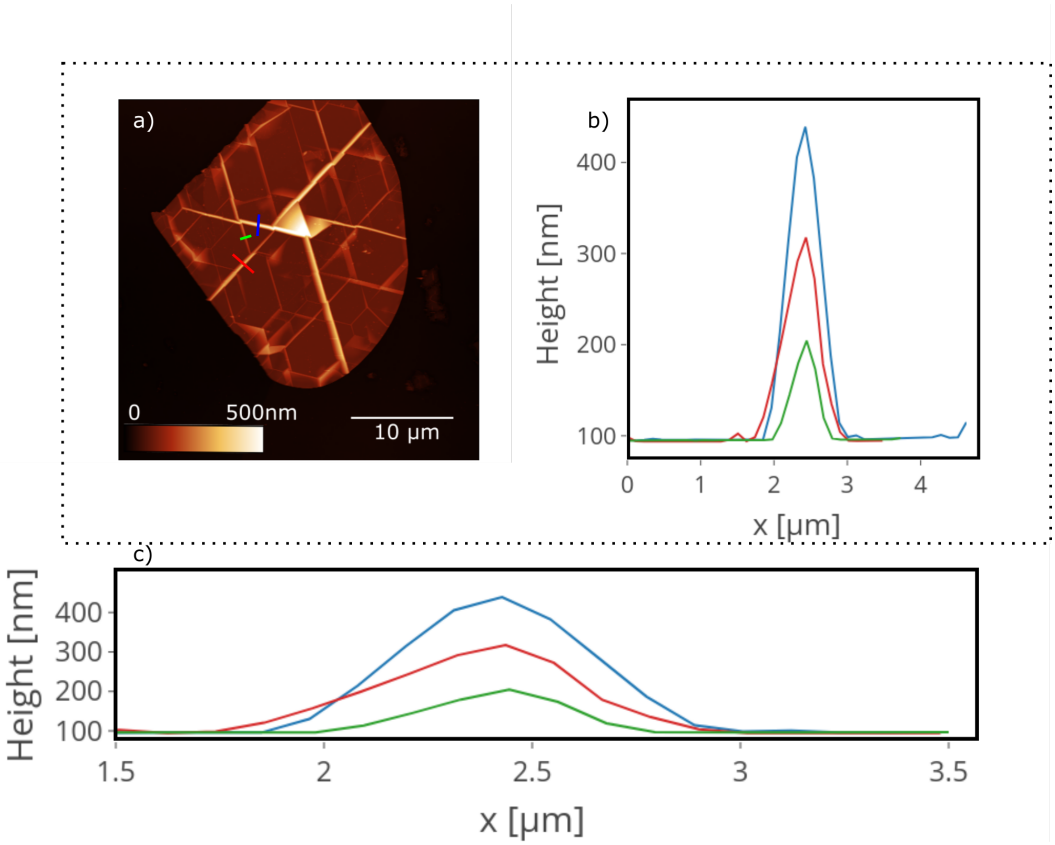

FIGURE 3.4: Wrinkles profiles. **a** AFM topography flake with the locations of the extracted line profiles in blue, red and green. The same colours have been used in for the corresponding profile plots on **b** and **c**. **c** displays the line profiles with same horizontal and vertical scales.

As it can be seen on the figure 3.4, a wrinkle can reach up to hundreds of nanometers high for around 1 micrometer wide. Those dimensions change with the thickness of the flake as it will be shown in the following figures.

Wrinkles aspect ratio We are now focusing on the aspect of the wrinkle itself. To do so, we also use a map of the flake acquired by AFM (still in tapping mode). We extract the profile of several wrinkles in several flakes and define the aspect ratio as the proportion between the height of the wrinkle and its full width at half maximum (see figure 3.5). Typically, the range of the aspect ratio goes from 0.01 to 0.5.

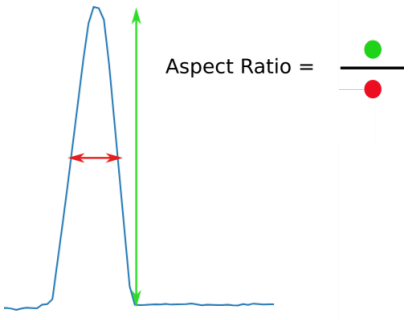

FIGURE 3.5: Wrinkles aspect ratio

Thickness of the flakes A relation between the aspect ratio of the wrinkles and the thickness of the flake they are found upon has been observed. The data have been extracted by AFM on several flakes (with different thicknesses) treated according to the same thermal process. Indeed the shape of the wrinkles changes as the flake thickens. By relying on the profile of the flake on the figure 3.6-**e**, it is noticed that the wrinkles looses their symmetry. Moreover, their interactions are different as well. Plateaus are more present on thick flakes but totally absent on the thinner ones. Finally, several aspect ratios are found within the same flakes which does not seem very conclusive a priori. However, if the average value of these aspect ratios (per flake) is considered, it is found that these values tend to reduce as the thickness of the flake increases (see figure 3.6-**f**).

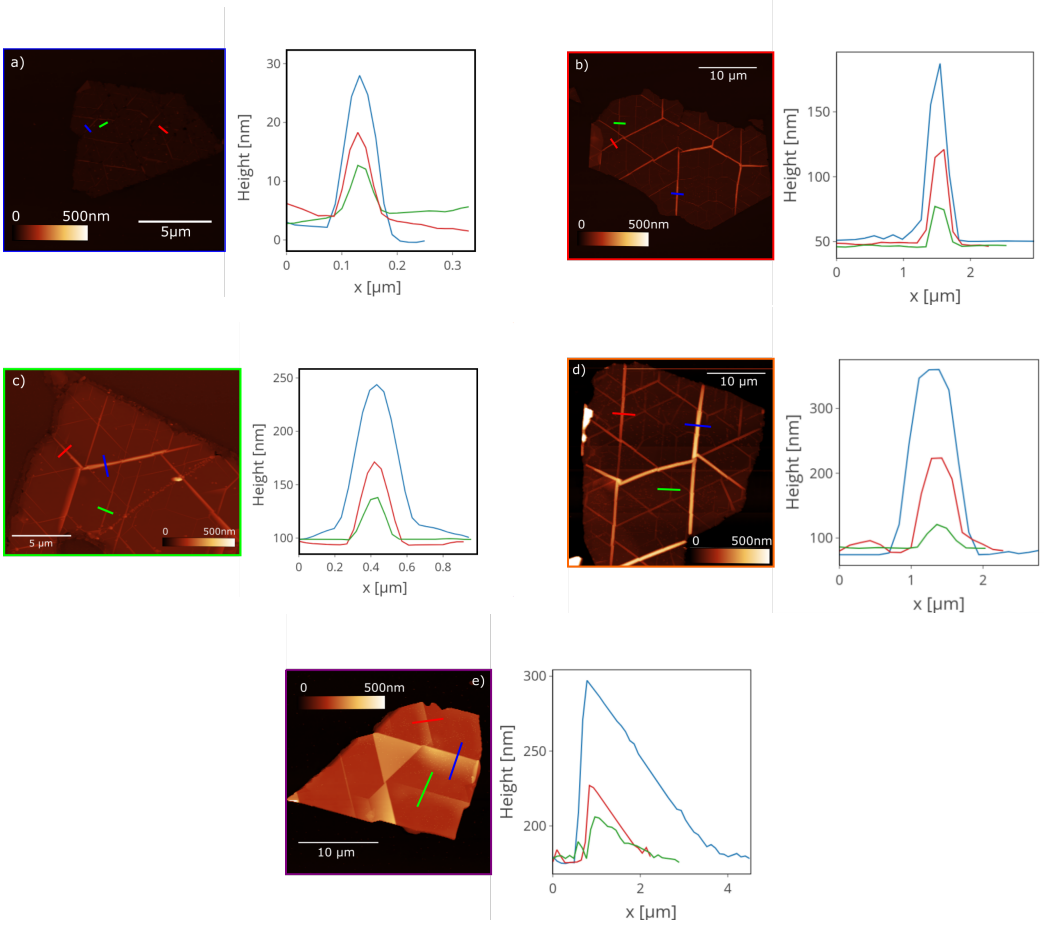

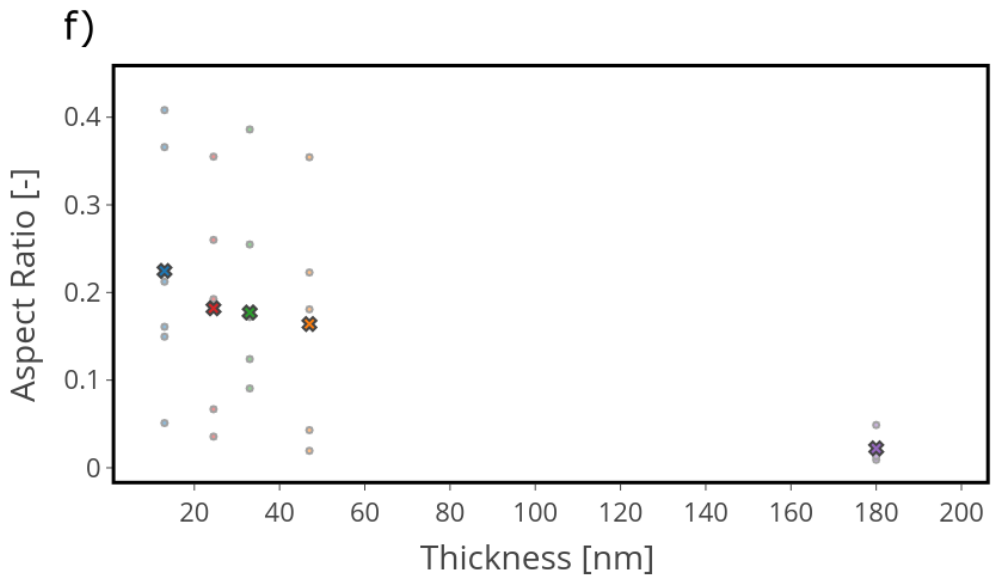

FIGURE 3.6: Wrinkles aspect ratio vs thickness. **a-e** Wrinkles profiles of hBN flakes annealed on BaF_2 at 990 °C with a 25 min duration of high-temperature plateau. Those flakes have different thicknesses: **a** framed in blue - 13 nm, **b** framed in red - 24.5 nm, **c** framed in green - 33 nm, **d** framed in orange - 47 nm and **e** framed in purple - 180 nm. **f** Dark crosses represent the average aspect ratio variation with the thickness of the flake. The dots represents the different values of aspect ratios measured on a flake of a given thickness and the crosses are the mean value of those aspect ratios. The colour of the dots and crosses match the colour of the frame of the flakes in the previous subfigures.

Process variation To evaluate the impact of the process on the wrinkles, an image processing software -ImageJ- has been used. The wrinkles density of a flake was extracted after converting the AFM image into a black and white pixels image (see figure 3.7. An option allows to determine which zones of the picture will be formed by black pixels and which will not. Finally, the fraction of black pixels is calculating by the software. This ratio will be used as reference for the wrinkles density. Since it is not possible to only isolate the wrinkles on the black and white pixels image, some error is introduced and will be taken into account in the graph thanks to error boxes.

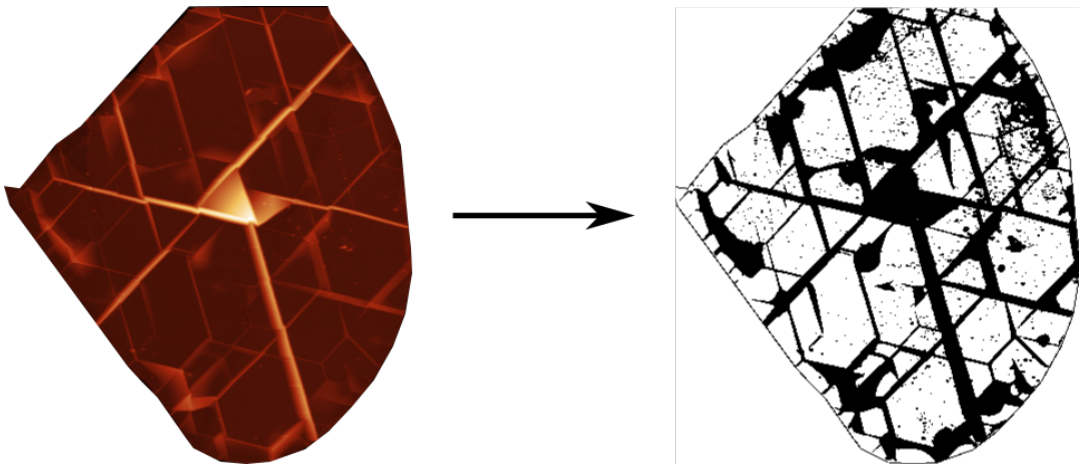

FIGURE 3.7: Image processing

The figure 3.8-**a** shows a general increase of the wrinkles density with the temperature. At lower temperature, wrinkles are observed only on a few flakes as it was the case at 500 °C. At

620 °C, no flakes with wrinkles were detected suggesting that the origin of the wrinkles at low temperature could be mechanical and occur during the exfoliation or transfer step of the process. Regarding the time, almost no change in the density is observed once it is superior to 5 minutes.

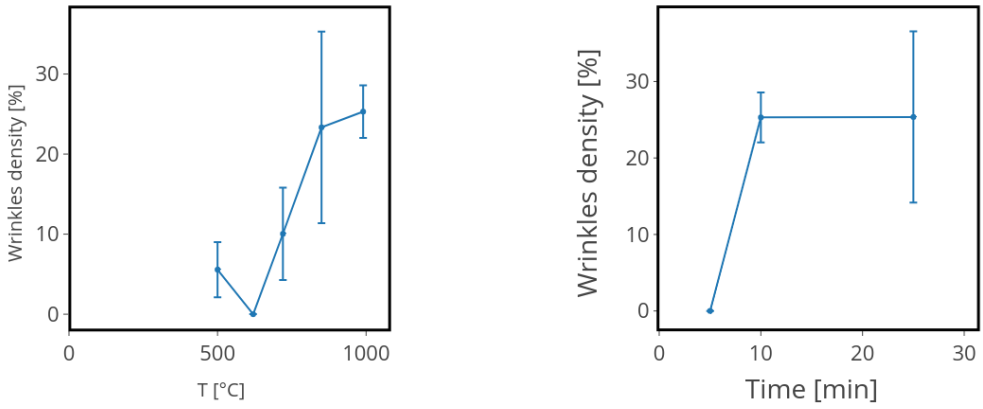

(A) (B)

FIGURE 3.8: Evolution of the wrinkle density with **a** the temperature (duration of the high-temperature plateau: 10 min) and **b** the duration of the high-temperature plateau (at 990 °C).

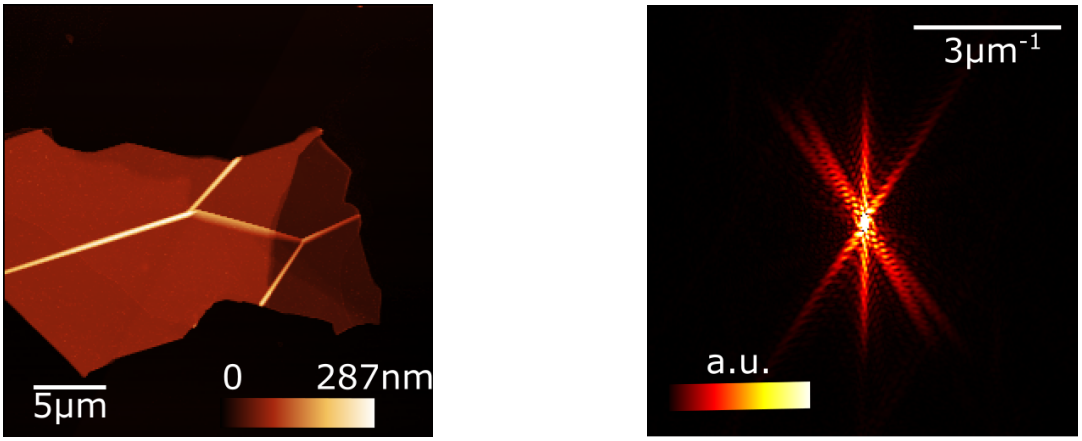

(A) (B)

FIGURE 3.9: Microscope images: **A** AFM map of an hBN flake on BaF_2 substrate. **B** FFT of the flake on figure **A**. The flake has been annealed at 720 °C for 10 min

After applying a FFT on several flakes, it is noticed that the orientation of the wrinkles is different (see figure 3.9) once annealed at a lower temperature (720 °C). The angles between the wrinkles are 30° and 120°. However, the time has no impact on the orientation. The figure 3.10 shows the same FFT for a flake that has been annealed at high temperature for 25 min as one annealed at high temperature for 10 min (see figure 3.3).

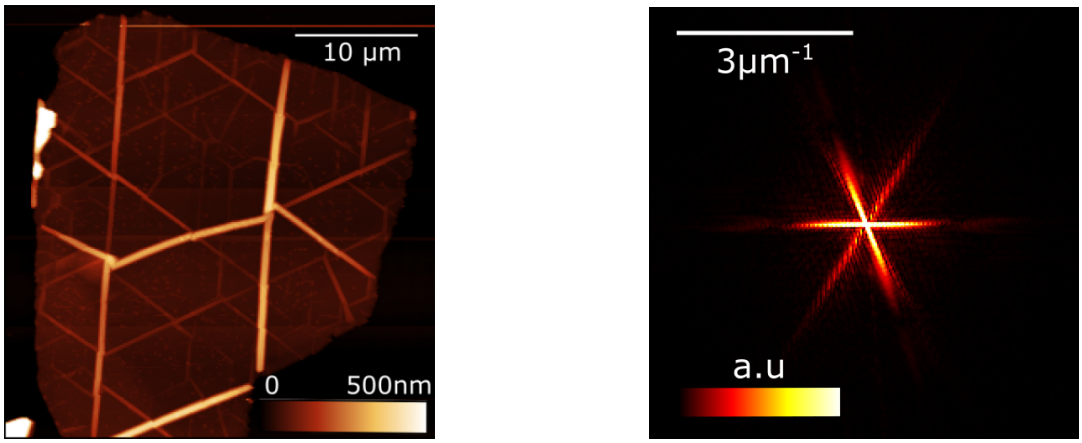

(A) (B)

FIGURE 3.10: Microscope images: **A** AFM map of an hBN flake on BaF_2 substrate. **B** FFT of the flake on figure **A**. The flake has been annealed at 990 °C for 25 min

3.1.2 Wrinkles junctions

In this subsection, we will present typical junctions that have been encountered during the measurements (see figure 3.11).

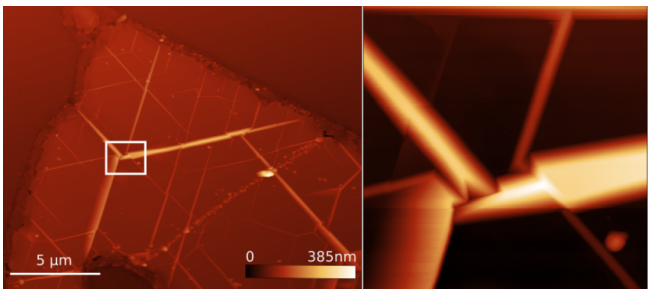

(A)

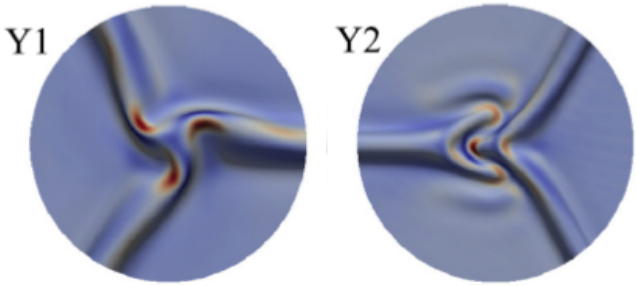

(B) (C)

FIGURE 3.11: Wrinkles junctions: 3-branches junction. **A** AFM image. **B** and **C** predicted configurations [20]

The first junction encounters is a typical Y-junction formed by three wrinkles. As compared to the predicted Y-junctions in the model presented section 1.2.1, it is noticed that none of them corresponds to the observed junction. In the experimental figure 3.11-**A**, the wrinkles seem to stop in front of each other while they merge completely (figure 3.11-**B**) or partially (figure 3.11-**C**) in the model.

The junctions formed by four wrinkles are another type of junctions that have not been predicted. In the experimental results, two types are identified. The first one is a typical X with one wrinkle getting over another. A discontinuity occurs a the meeting point of the

wrinkles (see figure 3.12). The geometry of the second type is more peculiar (see figure 3.13-**Aii**. The wrinkles twist around each other as they meet.

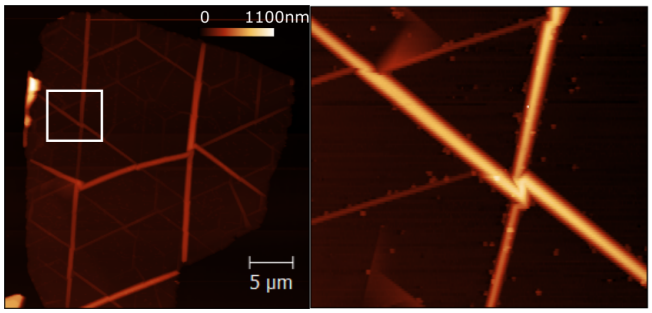

(A)

FIGURE 3.12: Wrinkles junctions: 4-branches junctions. **A** AFM image. **B** predicted configuration [20]

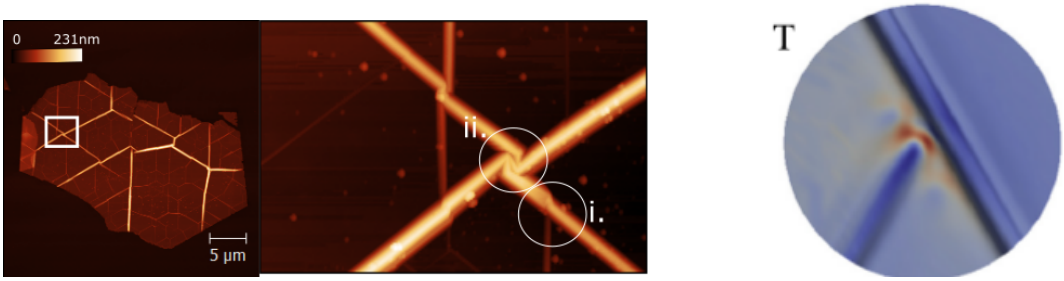

(A) (B)

FIGURE 3.13: Wrinkles junctions: T-junctions and 4-branches junctions. **A** AFM image. **B** predicted configuration [20]

In addition to those unexpected junctions, other predictions of the model have been observed. For example, the junction on the figure 3.13-**Ai.** corresponds to the T-junction presented. Moreover, a plateau (figure 3.14) has also been observed. However, some divergences are noticeable like the four wrinkles that form it or the presence of an adjacent plateau.

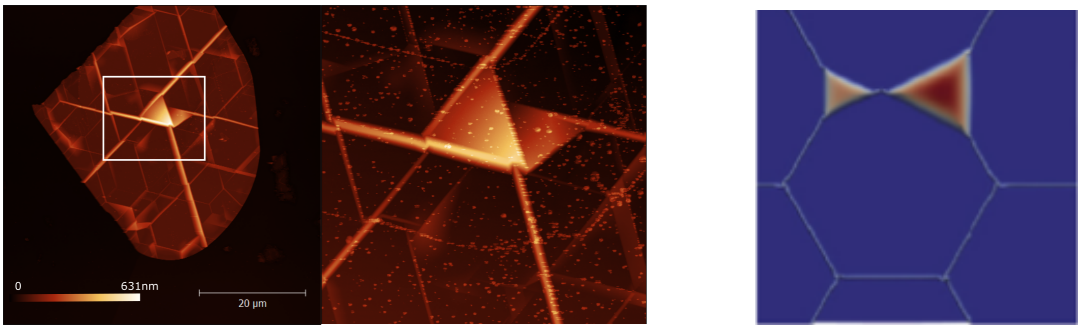

(A) (B)

FIGURE 3.14: Wrinkles junctions: Plateau. **A** AFM image. **B** predicted configuration [20]

3.2 Electrostatic observations

In order to evidence a polarization that could be associated with flexoelectricity due to wrinkling, several hBN flakes have been measured with an electrostatic force microscope (EFM, see subsection 2.3.2). The frequency shift (see figure 3.15) was mainly measured, since it appears to be more directly related to a surface polarisation or a surface charge (see equations 2.11) than the phase shift (see an example on figure 3.15). In addition, several measurements includes the variation of the potential of the tip. The measurements have been executed according to the two-steps procedure presented in subsection 2.3.2. In first instance, a lift of $60\,\mathrm{nm}$ in frequency shift and $80\,\mathrm{nm}$ in phase shift have been randomly applied. Thereafter, in the interest of quality of the results, a lift of $150\,\mathrm{nm}$ has been selected.

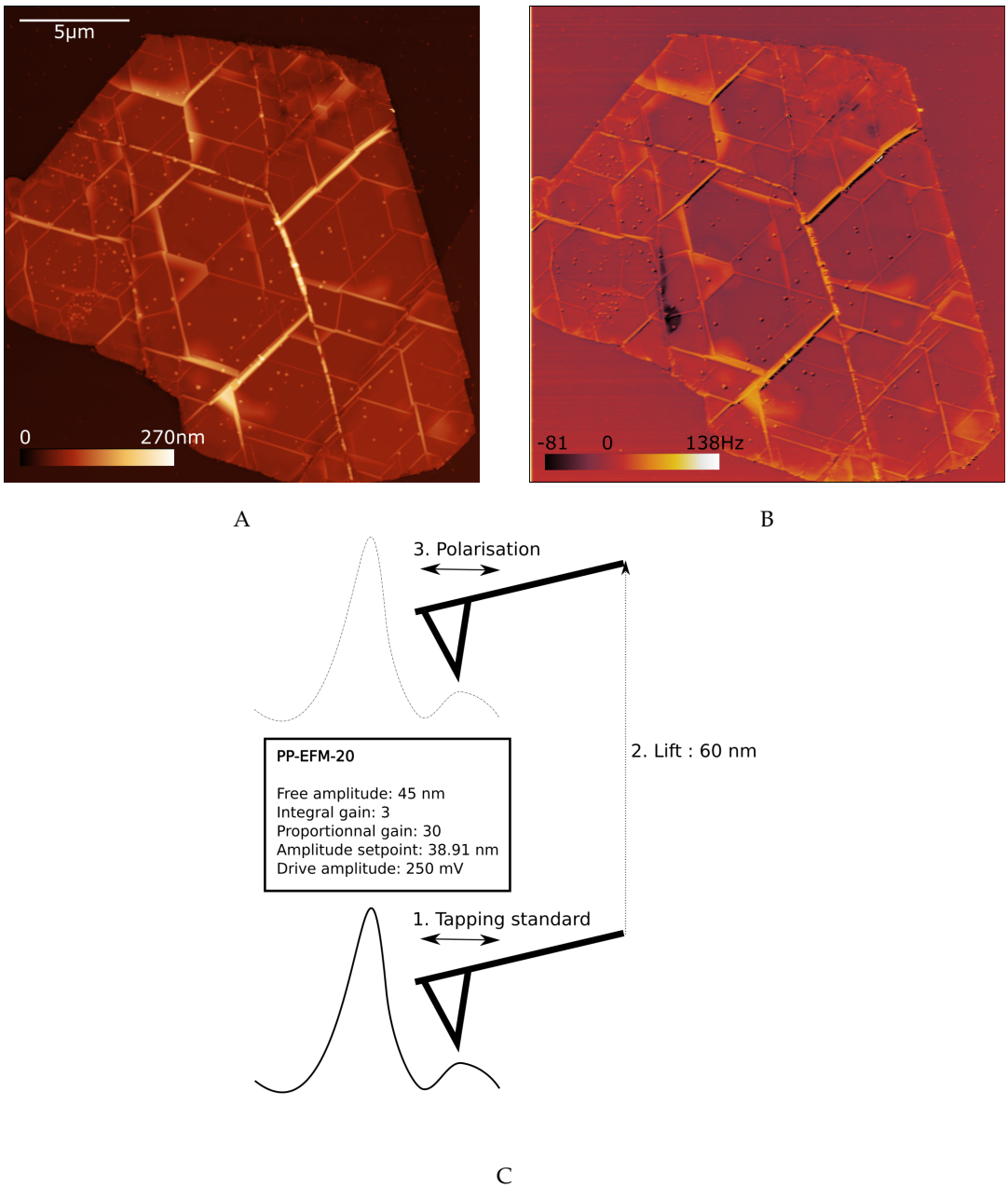

FIGURE 3.15: EFM measurements in frequency shift. **A** hBN Flake AFM topography. **B** EFM image of the same area, displaying the frequency shift with $V_{tip} = -12V$. **C** Procedure and parameters. The frequency shift value is given by the colour scale on the images.

In general, the EFM images in frequency shift as well as in phase shift are pretty similar to the corresponding topographies.The first observation may appear as a surprise, if one considers that the topography should be absent in the EFM contrast (due to the dual-pass procedure), and that the flakes are constituted by a single homogeneous material. A frequency shift is noticed over the wrinkle areas. It can be seen that the higher is the wrinkles, the stronger is the shift. Moreover, shifts are also observed over the particles present on the flakes. Figure 3.15-**A** and figure 3.15-**B** depict well this observation. Moreover, the suspended flat triangular zone in the topography presents a significant contrast in the phase. Unfortunately, the frequency shift has not been extracted for this zone of the flake. The result could have indicated whether the curvature of the flake is associated to a contrast in the frequency shift. Figure 3.15-**D** illustrates in particular the effect of the tip polarization on the EFM frequency shift contrast. The tip voltage was modified along the vertical axis of the image, during the scan. Figure 3.15-**D** also illustrates that the "topographic" contrast in EFM disappears in a range of voltage between $V_{tip} = 4$ and $6\,V$.

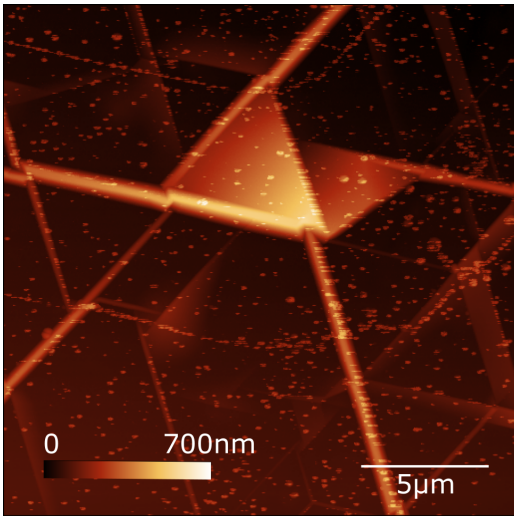

A

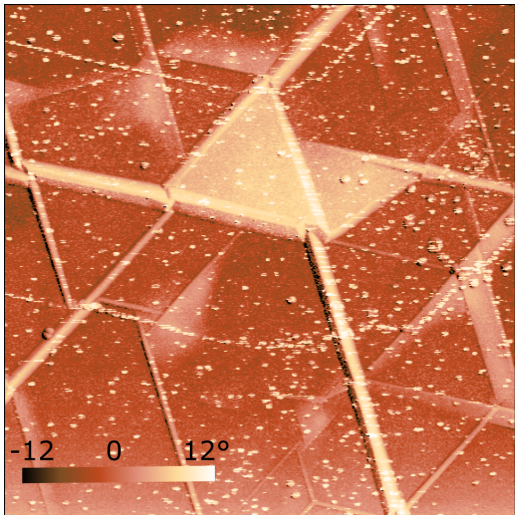

B

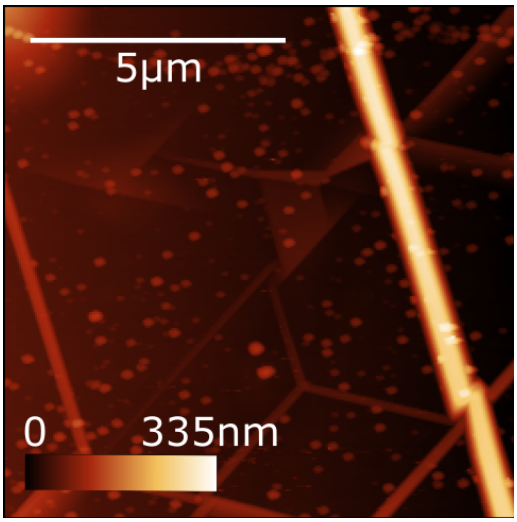

C

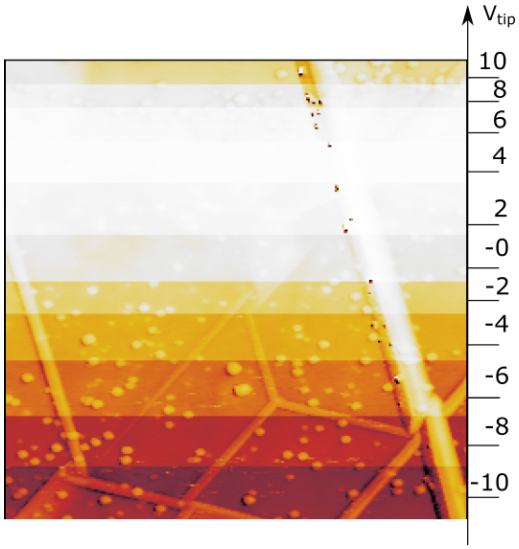

D

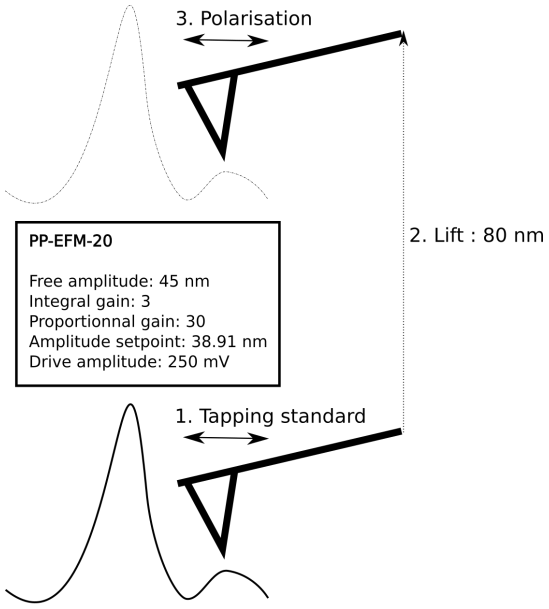

E

FIGURE 3.15: EFM measurements in phase shift and in frequency shift with potential tip variation. **A** and **C** hBN flake AFM topographies. **B** and **D** EFM images of the same areas, displaying respectively the phase shift and the frequency shift. **E** Procedure and parameters.

3.2.1 Variation of the potential

After optimisation of the topography parameters, the tip is lifted $150\,\mathrm{nm}$ above the sample at each line scan. The potential applied on the tip goes from $-10\,\mathrm{V}$ to $10\,\mathrm{V}$ (see figure 3.16-**B**). The variation of the EFM signal with the voltage applied of the flat and high (or top of wrinkles) regions can be seen on the figure 3.16-**C**. Both of the curves follow a quadratic evolution with the voltage as expected. The shift in the minimum potential $\Delta \mathrm{V}_{min}$ has a value of $0.675\,\mathrm{V}$. On the figure 3.16-**B**, the EFM contrast on the flake becomes featureless when the voltage on the tip goes from $0\,\mathrm{V}$ to $2\,\mathrm{V}$ but as on the previous figure (3.15), the features reappear as the voltage evolves. The evolution of the contrast in the frequency shift with V_{tip} seems parabolic with a maximum in a range going from $\mathrm{V}_{tip} = 0\,\mathrm{V}$ to $\mathrm{V}_{tip} = 2\,\mathrm{V}$. A shift in the maximum of this parabola is noticed if figure 3.16-**B** is compared to figure 3.15-**D**. This shift could be due to the difference in the lift (as a reminder, the tip was lifted at $150\,\mathrm{nm}$ in figure 3.16-**B** and at $80\,\mathrm{nm}$ in figure 3.15-**D**). Another difference that could explained this shift is the height of the wrinkles scanned (up to $240\,\mathrm{nm}$ in figure 3.16-**B** and at $335\,\mathrm{nm}$ in figure 3.15-**D**. The first assumption seems unlikely as the equation 2.11 is considered. Indeed, the frequency shift follows only a $1/z^3$ dependence. Regarding the second assumptions, more data will be analysed.

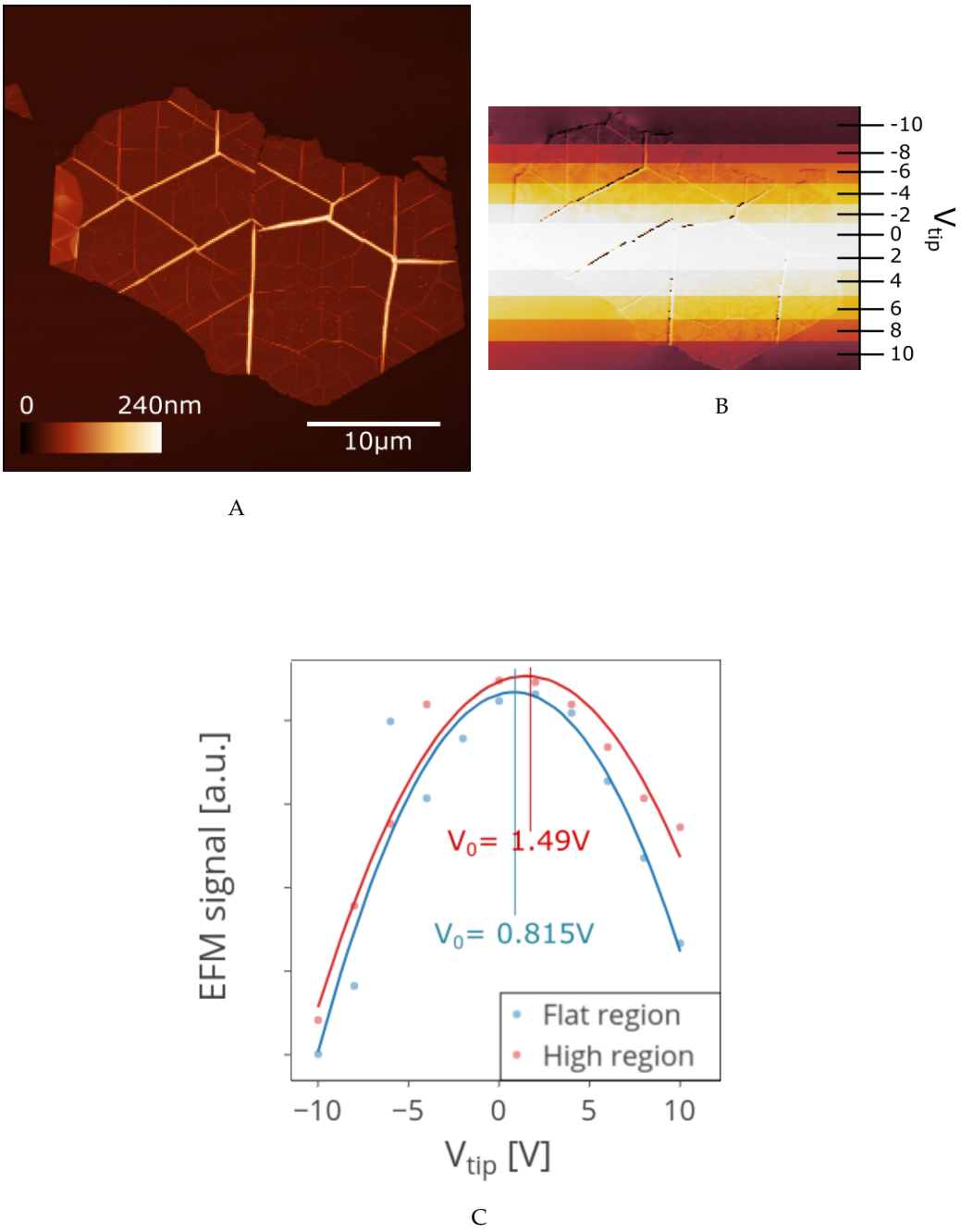

A B C

FIGURE 3.16: Potential variation. **A** Flake topography. **B** EFM image. **C** Variation of the baseline frequency with the tip potential

To have an idea of the frequency shift intensity at a given voltage, a flake has been scanned several times with different potential applied on the tip (see figure 3.17). It is seen that the value of the shift can attain $5\,\mathrm{Hz}$ and $4\,\mathrm{Hz}$ for the highest wrinkles as the voltage is respectively $-5\,\mathrm{V}$ and $5\,\mathrm{V}$ on the tip. Besides, the images are very alike with almost the same range of the frequency shift. As the potential on the tip amounts $0\,\mathrm{V}$, the range of frequency shift is more reduced. Even though the colour scale indicates a maximum of $4\,\mathrm{Hz}$, the colour of the flake shows a value closer to $0\,\mathrm{Hz}$ for the highest wrinkles. Figure 3.17-**D** illustrate that as well by giving the standard deviation of the frequency shift of the dotted framed zone in figure 3.17-**A**.

In figure 3.17-**A**, the EFM signal presents a significant contrast in a flat zone of the flake (see white framed area). This indicates an inhomogeneity in the surface potential that could be due to the progressive adsorption of several molecules such as water.

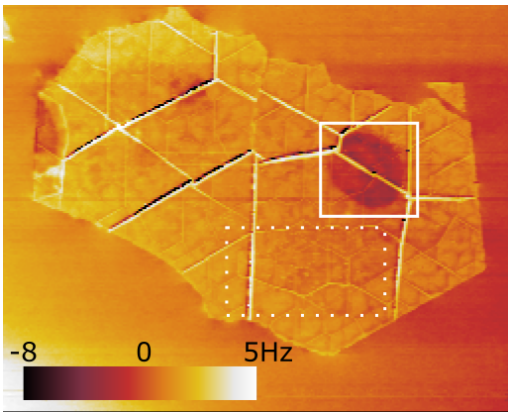

A: $V_{tip} = -5\,V$

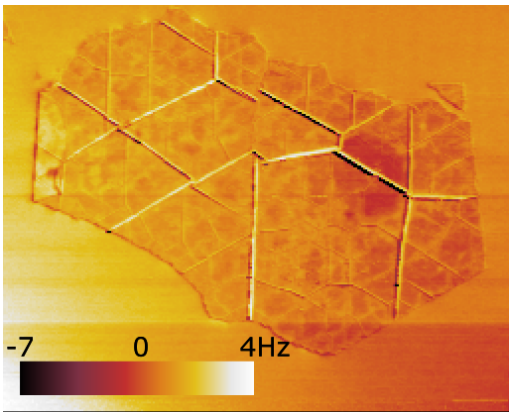

C: $V_{tip} = 5\,V$

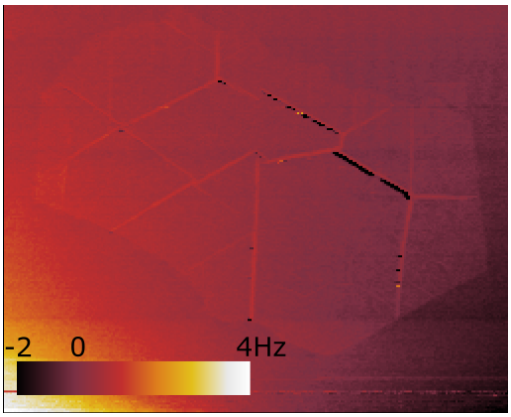

B: $V_{tip} = 0\,V$

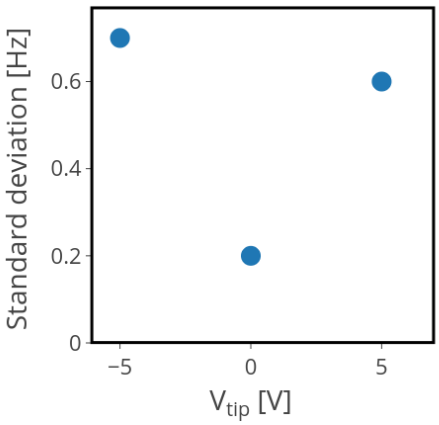

D: Standard deviation of the dotted framed zone on the flake in **A** for $V_{tip} = -5, 0, 5\,V$.

FIGURE 3.17: Frequency shift intensity

3.2.2 Wrinkles aspect ratio/height variation

Our previous results seem to indicate that there is a difference in the frequency shift depending on the aspect ratio or the height of the wrinkles. Figure 3.18-**D** depicts the evolution of the frequency shift with the variation of the tip potential for different wrinkles. A fit corresponding to the parabolic function :

$$\Delta f = -0.25C(V_{tip} - V_{min})^2 \tag{3.1}$$

has been applied to the actual data. From this fit, the curvature C and the minimum potential V_{min} are extracted. The standard deviation error for each parameter and for each wrinkles are given in table 3.18-**E**. As the curvature is plotted according to the aspect ratio (see figure 3.19-**A**), it is noticed that the latter increases as the curvature C of the parabola increases. The comparison between the shift in the curvature between 2 different wrinkles and the standard deviation errors allows us to qualified this evolution as significant. The evolution of the curvature with the height of the wrinkles has been also examined. It is illustrated on figure 3.19-**B**. The tendency is the same as on figure 3.19-**A**.

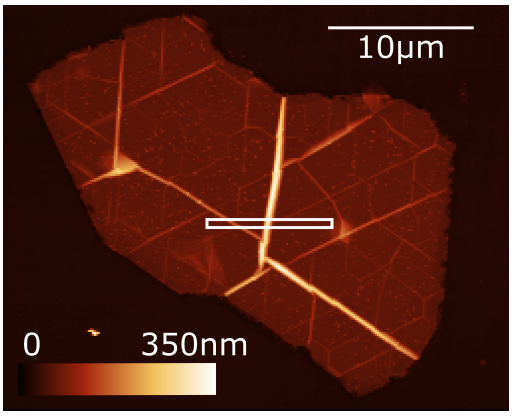

A

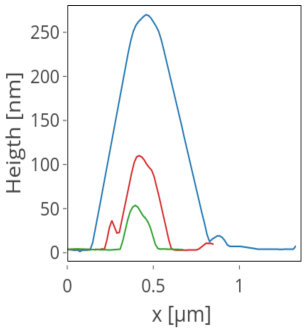

B

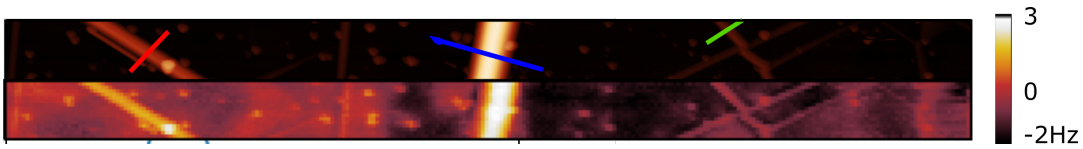

C

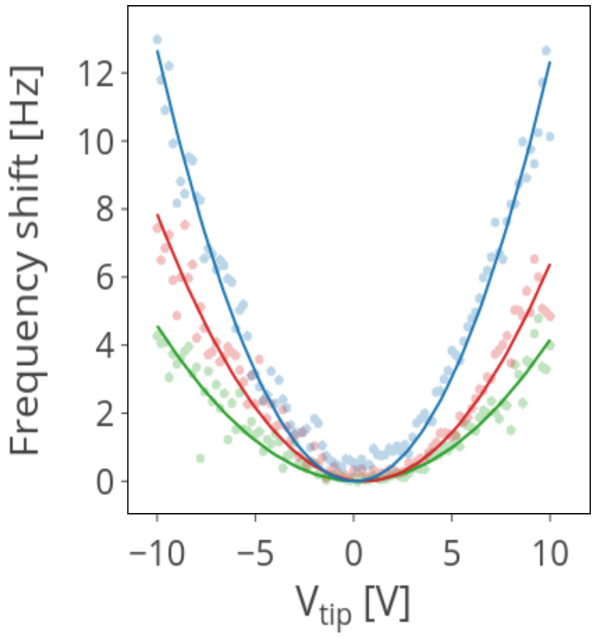

D

Standard deviation error		
Fitting parameters	C	V_{min}
AR_{blue}	0.006	0.045
AR_{red}	0.005	0.064
AR_{green}	0.004	0.084

E

FIGURE 3.18: Frequency shift vs V_{tip} for several wrinkles. **A** hBN flake topography. **B** Profiles of wrinkles indicated by the coloured lines in **C**: $AR_{blue} = 0.67$, $AR_{red} = 0.53$, $AR_{green} = 0.38$. **C** Zoom of zone framed in **A** with its EFM image. **D** Frequency shift vs V_{tip} for the wrinkles presented in the previous subfigures. **E** Standard deviation errors of the fitting parameters. Thermal treatment: 25 min at 990 °C

The evolution of the minimum potential V_{min} does not seem to follow a monotonic trend (see figure 3.19-**C**. As the standard deviation error is compared to the shift of the extracted values for V_{min} between 2 different wrinkles, it is realised that the results are significant. The evolution of the minimum potential with the height of the wrinkles has been also treated. It is depicted on figure 3.19-**D**. The tendency is the same as on figure 3.19-**C**.

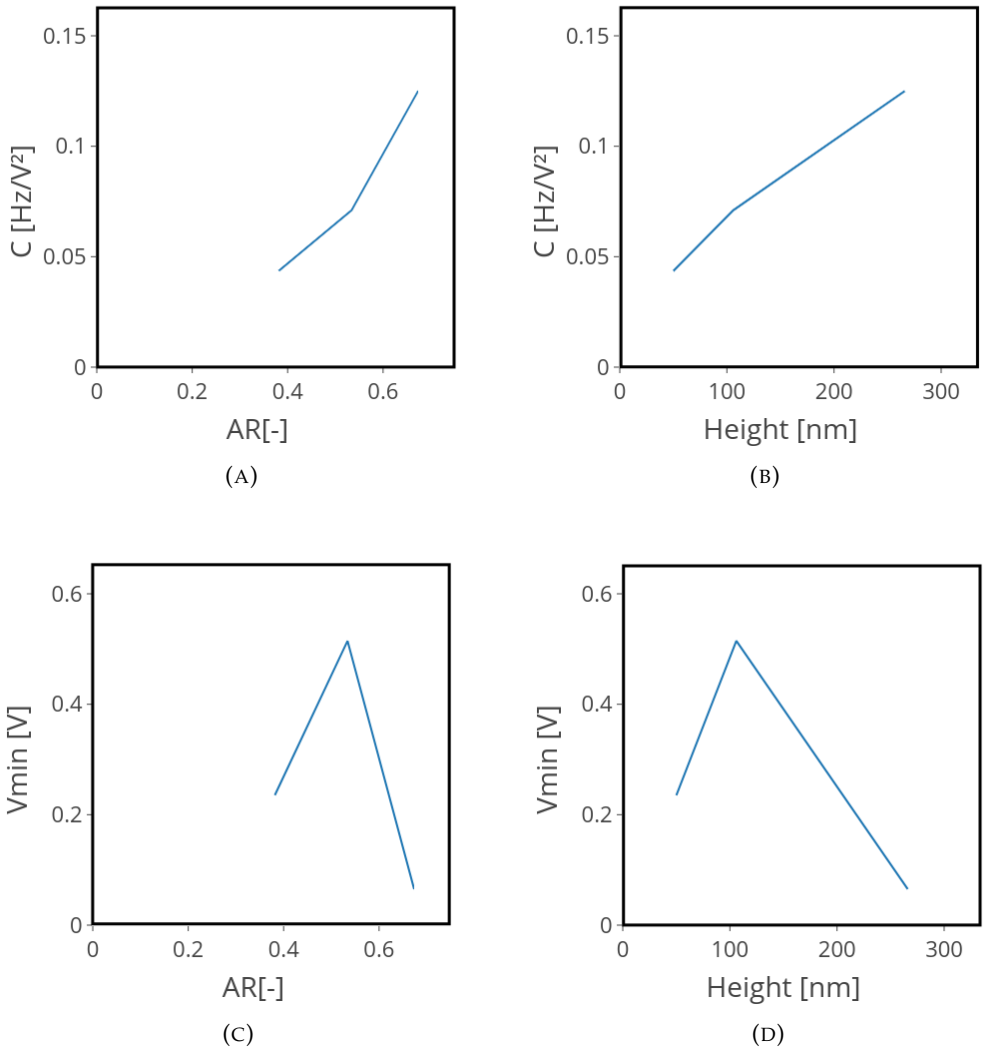

FIGURE 3.19: Evolution of fitting parameters C and V_{min}: parameters extracted from the fit of the frequency shift on figure 3.18. **A** C vs aspect ratio of the wrinkles. **B** C vs height of the wrinkles. **C** V_{min} vs aspect ratio. **D** V_{min} vs height.

The EFM signals of the a flat region of the flake and a high region (or top of a wrinkle) are also been extracted. The tendency of the evolution with the V_{tip} seems quadratic in a range that goes from $V_{tip} = -10\,V$ to $V_{tip} = 0\,V$. However, at $V_{tip} = 0\,V$, an unexpected jump in the data is noticed and the tendency becomes more linear.

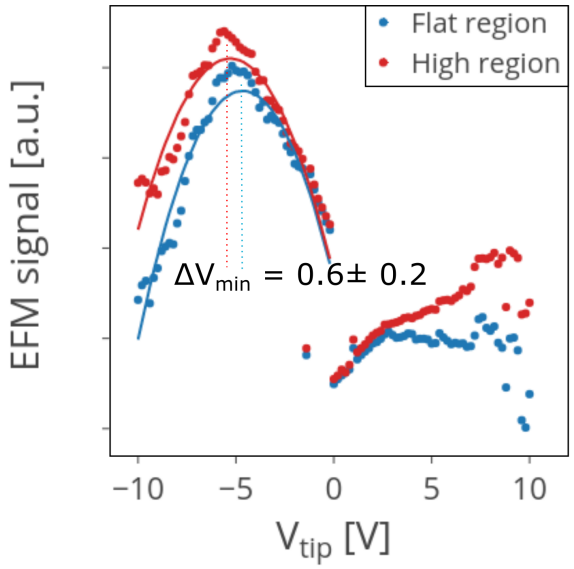

FIGURE 3.20: EFM signals of flat and high regions of the flake on figure 3.18-**A**

3.2.3 Metallisation impact

The same kind of data have been extracted from a metallized flake (see figure 3.21). The flake has been metallized in order to screen the potential due to the possible polarisation around the wrinkles. Therefore, only the information due to the flake geometry are supposed to be recorded by the tip. Hence, $2.5\,\mathrm{nm}$ of Ni followed by $15\,\mathrm{nm}$ of gold has been deposited on a flake annealed in the same condition as previously ($25\,\mathrm{min}$ at $990\,^{\circ}\mathrm{C}$).

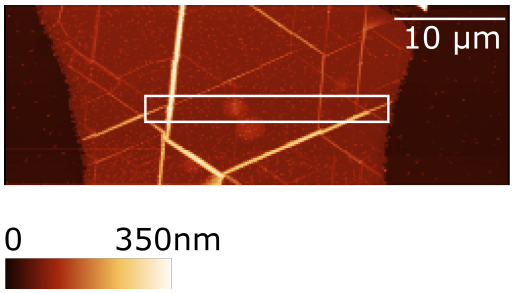

A

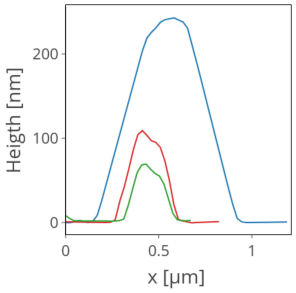

B

C

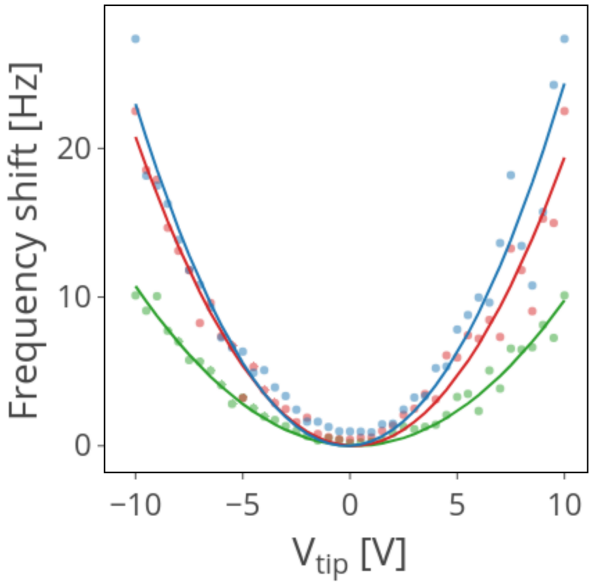

D

Standard deviation error		
Fitting parameters	C	V_{min}
AR_{blue}	0.026	0.112
AR_{red}	0.019	0.095
AR_{green}	0.008	0.076

E

FIGURE 3.21: Frequency shift vs V_{tip} for several wrinkles of a metallized flake. **A** hBN flake topography after metal deposition. **B** Profiles of wrinkles indicates by colour in **C**: $AR_{blue} = 0.57$, $AR_{red} = 0.54$, $AR_{green} = 0.34$. **C** Zoom of zone framed in **A** with its EFM frequency-shift image. **D** Frequency shift vs V_{tip} for the wrinkles presented in the previous subfigures. **E** Standard deviation errors of the fitting parameters. Thermal treatment: 25 min at 990 °C

The aspect of the curves is similar to the one obtained on the non-metallized flake. The parameter C evolves likewise but on a higher scale. It is also observed that minimum potential increases with the aspect ratio while the curvature acts as for the non-metallized flake (see figure 3.22). However the intensity of the shift in V_{min} is stronger. The figures 3.22 depict the tendency of the C and V_{min} parameters of the metallized flake depending on the aspect ratio and the height. The figures 3.23 illustrates the comparison between the case of the metallized and normal flake.

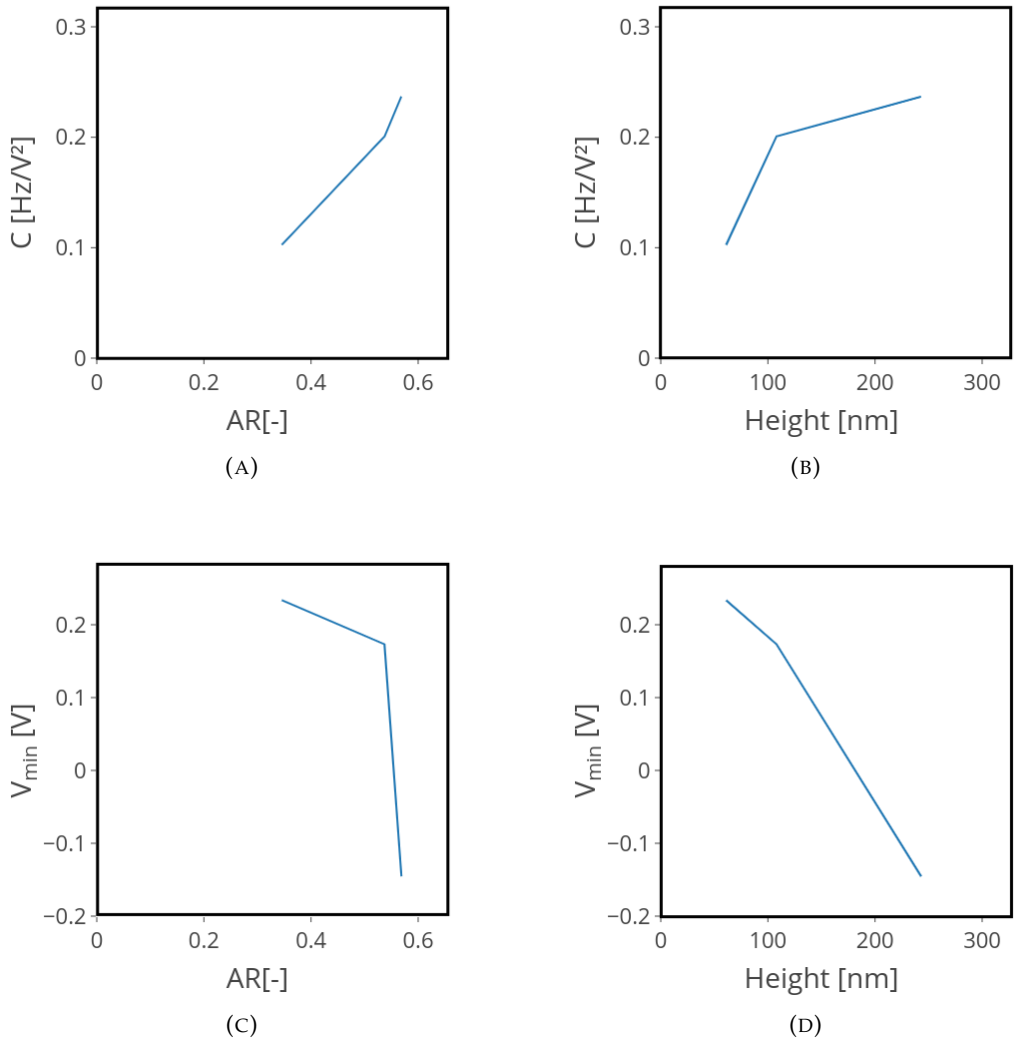

FIGURE 3.22: Evolution of fitting parameters C and V_{min}: parameters extracted from the fits of the frequency shift on figure 3.21. **A** C vs aspect ratio of the wrinkles. **B** C vs height of the wrinkles. **C** V_{min} vs aspect ratio. **D** V_{min} vs height.

The EFM signal of the high and flat regions have also been extracted. In this case, a quadratic relation with the potential of the flake is found (see figure 3.24). The shift in V_{min} is equal to (0.22 ± 0.02) V. This is significantly smaller than the shift in V_{min} found in a non-metallized flake (0.675 V in figure 3.16 and almost 0.63 V in figure 3.20). Although a statistical analysis of ΔV_{min} on several flakes would be needed to confirm the trend, such a difference may indicate that there is indeed a polarization at the top of the wrinkles, measured by V_{min}. Again, this important results is still preliminary, and it was not possible in this thesis to repeat this type of measurement more than three times. (note that to measure data such as in figure 3.18, 100 scans of a few lines have been measured, changing the tip voltage manually.This corresponds to approximately one day of measurements). Note also that, ideally, the comparison of ΔV_{min}

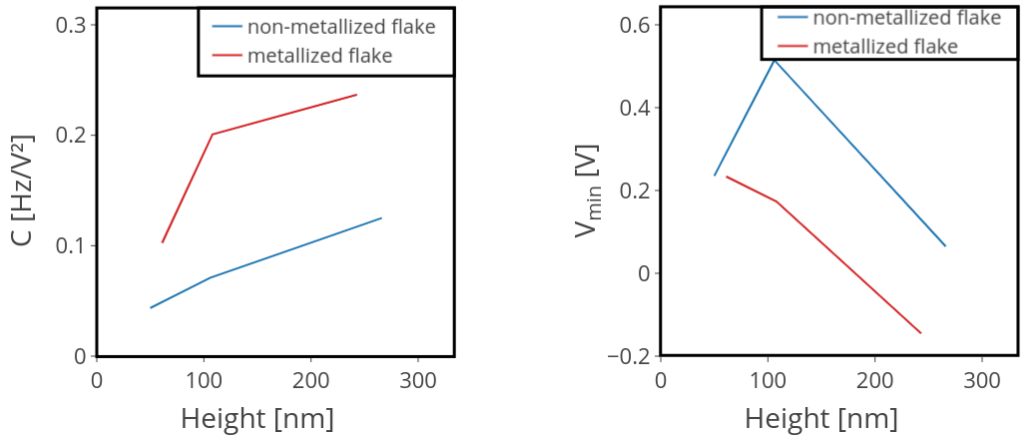

(A) (B)

FIGURE 3.23: Evolution of fitting parameters C and V_{min}: parameters extracted from the fits of the frequency shift on figures 3.18 and 3.21. **A** C vs height of the wrinkles. **B** V_{min} vs height.

between the flat and wrinkled region should be performed on the same region of the same flake (it is not always the case here).

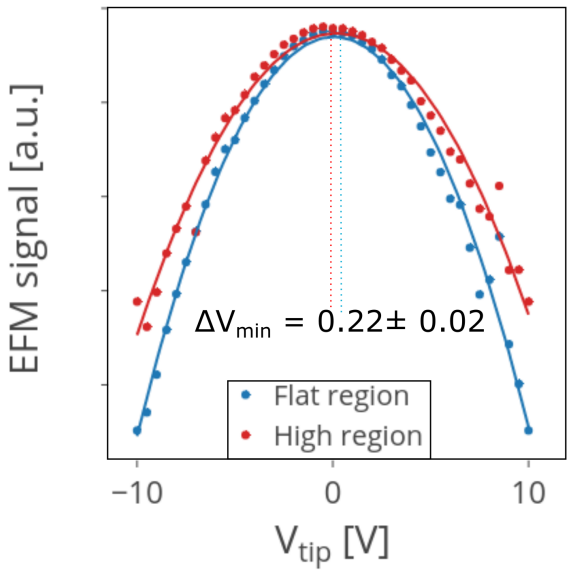

FIGURE 3.24: EFM signals of flat and high regions of the metallized flake on figure 3.21-**A**

Chapter 4

Discussion

4.1 Topography

4.1.1 Wrinkles aspect and tip-induced deformation

As presented in the previous chapter, the shape of a wrinkle could be described as hilly with a height that can go over a hundreds of nanometers. Within a single flake, several wrinkles with different aspect ratios are observable. In general, an equivalence between the wrinkles with respect to their aspect ratio has been noticed. It is possible to classify the wrinkles into several subnetworks. Having in mind the dimensions of the tip and comparing them with the possible dimensions of the wrinkle, one may wonder if the profile extracted would not have been altered by tip artifacts. In some cases, the effect is easy to detect as on figure 4.1 which depicts a flake scanned by a double-tip. As it can be seen, all the wrinkles appear twice. It is also the case of the particles located outside of the flake.

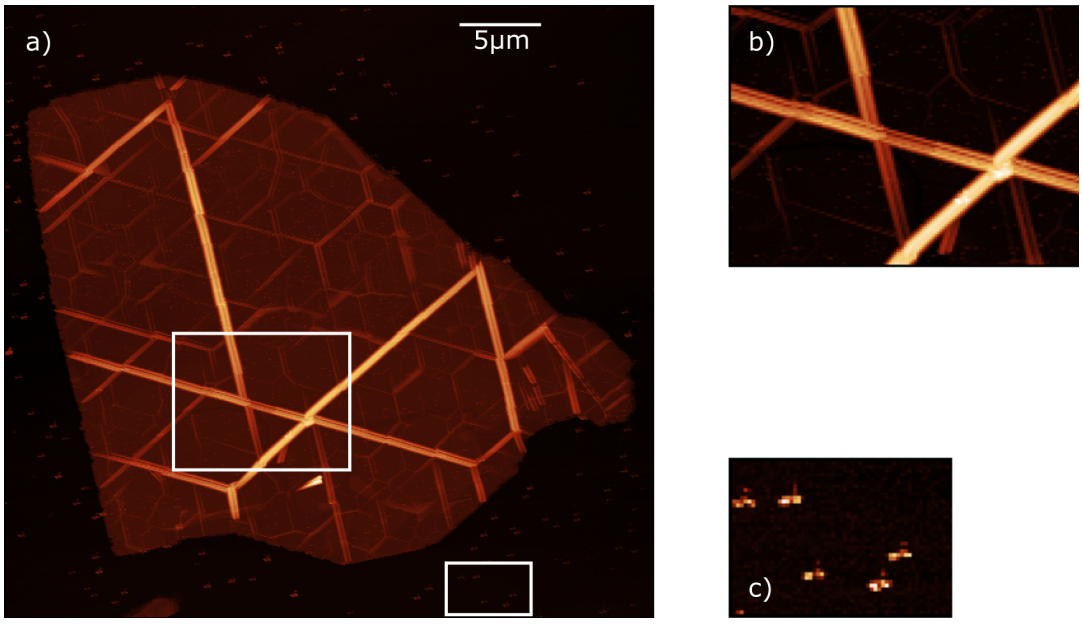

FIGURE 4.1: Double tip effect on hBN flake (**a**) with a zoom on the framed zones in (**b**) and out (**c**) of it.

Concerning convolution effect, it possible to correct the data thanks to some algorithms which take into account the shape and the type of the probe [44]. In our case, the adjusted results were quite similar to the original ones. Therefore, it has been decided to neglect this effect.

Besides the profile of the wrinkle, not much information regarding its precise geometry are provided. Indeed, the wrinkles could be cracked on the top or folded somehow. Even though we cannot resolve details smaller than the tip apex (around 10-20 nm), we could identify

general trends. It is the case of the evolution of the aspect ratios with the thickness of the flakes. Even though there is a dispersion of our aspect ratio data depending on the flakes, in average, it is found that these aspect ratios tend to reduce as the thickness of the flake increases (see figure 3.6).

4.1.2 Wrinkles formation

The models presented on the section 1.2.1 for the graphene could explain the formation of wrinkles in hBN flakes on a BaF_2 substrate. Indeed, the origin of the wrinkling of hBN would be due to an isotropic compression. As explained on the subsection 1.2.2, the compression is the result upon cooling of the opposite signs of the thermal expansion coefficients of the flakes and the substrate. Like Si, BaF_2 has a positive thermal expansion coefficient. Moreover the value of the latter is superior to the one of the Si, so, as a result, the wrinkles formed on BaF_2 have higher aspect ratios. Indeed, if we rely on the following equation:

$$\epsilon = \Delta\alpha\Delta T \tag{4.1}$$

which depicts the strain due to temperature change in an isotropic case, we see that an increase of $\Delta\alpha$ results on an increase of the strain.

The influence of the temperature is very clear and is consistent with our hypothesis. By lowering the annealing temperature, we reduce the strain and therefore the density of the wrinkles. Regarding the duration of the high-temperature plateau, it is expected by considering the absence of temporal dependence in the equation and assuming that the wrinkles are formed upon cooling, that it should have no influence on their generation. Our results show that that fact is partially true. Indeed, above a certain threshold, the density of wrinkles almost does not vary. However, if the time spent at the maximum annealing temperature is below this threshold, no deformation is found in the flake. This suggests that wrinkle formation takes its origin during the initial phase of the plateau at high temperature. The scenario that we propose is the following. Somehow, at high temperature, the flakes, whose size tends to shrink, while the substrate is expanding, have to slide and contract with respect to the substrate as soon as their elastic deformation becomes insufficient to accommodate the expansion of the substrate. This relative dissipative sliding or slipping motion may take some time to occur (which would explain the threshold). Then, upon cooling, the sliding motion becomes less favourable than at high temperature. Therefore, as the substrate is contracting and the flake is anchored on the substrate, the only way to accommodate the constraint is to deform in the out-of-plane direction and form wrinkles.

There are several aspects of the formation of the wrinkles that the models do not explain. First, the orientation of the wrinkles are indeed not random. Nonetheless, it seems to evolve at lower annealing temperature: for a low-temperature annealing, the orientation tends to be more random. Besides, no clear relation with the crystallographic orientation has been detected. Indeed, the straight sides of the flakes can be considered as parallel to the principal axes. On the figure 3.3-**A**, no wrinkles are parallel to the straight sides of the flake. It is also the case on the figure 4.1. However, an hypothesis that could explain the particular orientation of the wrinkles is that the wrinkles orientation would be related to the crystallographic orientation of the substrate. Moreover, in the case the crystallographic orientation of the flake does not matter, we could assume that the mechanical properties of the flakes are isotropic.

Second, the influence of the thickness of the flakes has not been treated up to now. It is not easy to identify whether the whole flake is wrinkled (all the layers from the bottom to the top) or only some layers on the top of it. The first idea seems to be the most consistent with our observations. Indeed, the compression strain is induced by the substrate which implies a deformation going from the bottom of the flake to the top. In that case, the width of a wrinkle should at least be twice the value of the thickness of its flake. After verification, it is observed that the width close to the top of the smallest wrinkles fulfil the requirement. This constraint could explain the decrease in the aspect ratio as the thickness increases. As explained before, we define the aspect ratio of a wrinkle as its height divided by its full width at half maximum.

By linking the width of a wrinkle to its thickness as we did, we obtained indeed that the aspect ratio is more likely to decrease with the thickness of the flake.

Finally, some of the wrinkles junctions correspond to the ones presented in the model in the subsection 1.2.1. We even find some plateaus, i.e. part of the flake is suspended at some distance from the substrate. However, it is difficult to determine whether those plateaus are due to the presence of fluids below the flake or due to another mechanism. Moreover, plateaus have been detected only on flakes with a thickness superior to $85\,\mathrm{nm}$ so this seems to indicate that such structures are not stable or at least not favoured on thin flakes. Regarding the origami junction in the model 1.2.2, it has not been observed, but there is also a large variety of junctions that we have observed, and that had not been predicted by this model, which leaves some room for future work to improve the model.

4.2 EFM contrast

Concerning the electrostatic observation, our results attest the presence of a clear EFM contrast between the flat region and the wrinkled region of the flake. As explained in the subsection 2.3.2, the evolution of the minimum potential V_{min} of the wrinkles extracted from the fitting of the data points points towards the presence of charges or dipoles on the wrinkles apex. Since V_{min} is different for several aspect ratios, it can be said that the intensity of the charges/dipoles depends on it. Nonetheless, the relation between the two stays indeterminate. The figures 3.19 and 3.22 depict different types of variation. Note also that a significant EFM phase shift contrast has been also observed on a flat, but suspended surface, which means that wrinkles curvature is not the only parameter that plays a role in the formation of the EFM contrast. Regarding the factor C, its evolution with the aspect ratio implies a change in the capacitive system. Indeed, if we refer to the capacitive model developed in subsection 2.3.2

$$C = \frac{\omega_0}{k}\frac{\epsilon A}{z^3} \tag{4.2}$$

and is supposed to be constant. Nevertheless, in this model, the tip interacts with a plane surface which was not our case. Since the distance $z = 150\,\mathrm{nm}$ is fixed, the dielectric constant ϵ depends on the medium (air - which did not change either) and the resonance frequency as well as the spring constant are related to the tip, only a change in the area could explain this variation. The fact that C decreases with the aspect ratio weighs in favour of this explanation.

Even though our results tend to point towards the presence of dipoles or charges at the wrinkles apexes, their origin is still difficult to determine and cannot be attributed for sure to flexoelectricity (also because a strong contrast is observed on suspended parts of the hBN flakes, where no strain gradient is present). Indeed, the figures 3.15 and 3.15 show that the contrast is not only present over the wrinkles but also over particles present on the flake. The origin of those particle is unclear but could be related to the exfoliation step where the scotch tape is in contact with the flake. An EFM contrast in this case could stem from the fact that particles are not composed of hBN, and therefore have a different work function from that of the hBN. Since the EFM signal is also sensitive to the work function, it is quite logical to observe an EFM contrast on top of such particles. Actually, the EFM signals obtained seem, in every case, to follow closely the topography of the flake. Every features of it can be seen on the corresponding EFM images. However, the measurements made on the metallized sample lead to a reduced value of the $\Delta\mathrm{V}_{min}$ between the flat and wrinkled regions of the flake. A metal layer was added in order to potentially screen the potential derived from the polarisation on the wrinkles. Unfortunately, not enough information has been recorded to confirm this observation and our hypothesis. Apart from that, the results obtained are similar to those in the normal case but with a stronger intensity. Note that the measurements have not been done on the same flake before and after metallisation. Besides, both the flake and its substrate are electrical insulators. The electrostatic potential of the sample was therefore not fixed during the procedures, in addition, there was no reference potential such as that

of the metal with a known work function that could be used to extract more quantitative information from the EFM measurements.

Conclusion

The main objectives of this thesis were to analyse the formation of a specific type of defect on a two dimensional material, characterise it and prove the existence of a certain property induced by its presence. We chose to concentrate our effort on the formation of wrinkles on hBN upon annealing and on the flexoelectricity that could come out of it. To do so, several experiments have been achieved. Several flakes, produced by exfoliation, have been annealed according to different thermal processes. Their topography was extracted by AFM measurement in tapping mode. Thanks to the results, correlations between different features have been discovered (temperature of the thermal process, density, aspect ratio of the wrinkles, thickness of the flakes, ...). EFM measurements allowed us to extract data regarding the potential variation of the flakes with their topography. In this context as well, some features also were linked.

Main observations

First, the formation of the wrinkles can be explained by several preexisting models established for graphene, provided that some adjustments are introduced. Nevertheless, some divergences still need to be explained such as the specific orientation of the wrinkle or the peculiar junctions shapes.

Afterwards, even though the profile of the wrinkle is reasonably well characterised thanks to the AFM measurements, no detailed information on the shape of the wrinkles are known, such as their internal structure, or the presence of cracks or peculiar folds in the vicinity of their apex. We observe, however that their aspect ratios, in average, reduce with the thickness of the flakes. Moreover, the importance of the temperature or the duration of the high-temperature annealing plateau is now highlighted. Indeed, their influence on the density is relevant.

Finally, a clear contrast in the EFM signal is detected between flat parts of the flake and the wrinkles, especially regarding the minimum potential shift (ΔV_{min}). Indeed, this shift is, a priori, reduced as the flake is metallized. Besides, the frequency shift increases with the aspect ratios of the wrinkles. Those result attest of the presence of charges or dipoles over the wrinkles area. Their origin stays, unfortunately, still unknown.

Prospects

As stated, lots of questions are still left unanswered and further experiments should be conducted to provide clarifications. One can also wonder about the influence of the wrinkles in general on other properties of the flakes. What can we expect from them in other two dimensional materials such the transition metal dichalcogenides? What other properties could they induce? Could they be used to extract mechanical properties of the material? One of the peculiarities of the two dimensional crystals is the possibility of building complex architectures, what could origamis bring in a heterostructure? How could we use the controlled high-temperature formation of wrinkles to build designed origami structures?

Bibliography

[1] Camilla K. Oliveira et al. “Crystal-oriented wrinkles with origami-type junctions in few-layer hexagonal boron nitride”. In: *Nano Research* 8.5 (2015), pp. 1680–1688.

[2] Pavlo Zubko, Gustau Catalan, and Alexander K. Tagantsev. “Flexoelectric Effect in Solids”. In: *Annual Review of Materials Research* 43.1 (2013), pp. 387–421.

[3] Florian Banhart, Jani Kotakoski, and Arkady V Krasheninnikov. “Structural defects in graphene”. In: *ACS nano* 5.1 (2010), pp. 26–41.

[4] Zhong Lin et al. “Defect engineering of two-dimensional transition metal dichalcogenides”. In: *2D Materials* 3.2 (2016), p. 022002.

[5] A. K. Geim and I. V. Grigorieva. “Van der Waals heterostructures”. In: *Nature* 499 (2013), 419 EP -.

[6] K S Novoselov and A H Castro Neto. “Two-dimensional crystals-based heterostructures: materials with tailored properties”. In: *Physica Scripta* 2012 (2012), p. 014006.

[7] D. D. L. Chung. “Review Graphite”. In: *Journal of Materials Science* 37.8 (2002), pp. 1475–1489.

[8] Matthew J. Allen, Vincent C. Tung, and Richard B. Kaner. “Honeycomb Carbon: A Review of Graphene”. In: *Chemical Reviews* 110.1 (2010), pp. 132–145.

[9] Wonbong Choi et al. “Synthesis of Graphene and Its Applications: A Review”. In: *Critical Reviews in Solid State and Materials Sciences* 35.1 (2010), pp. 52–71.

[10] C. N. R. Rao et al. “Graphene, the new nanocarbon”. In: *J. Mater. Chem.* 19 (2009), pp. 2457–2469.

[11] Andre K Geim and Konstantin S Novoselov. “The rise of graphene”. In: *Nature materials* 6.3 (2007), p. 183.

[12] A. K. Geim. “Graphene: Status and Prospects”. In: *Science* 324.5934 (2009), pp. 1530–1534.

[13] Jesus de La Fuente. *Graphene Applications & Uses*. https://www.graphenea.com/pages/graphene-uses-applications#.WuzRkqSFO00.

[14] Amir Pakdel, Yoshio Bando, and Dmitri Golberg. “Nano boron nitride flatland”. In: *Chem. Soc. Rev.* 43 (2014), pp. 934–959.

[15] Xiang-Fen Jiang et al. “Recent Progress on Fabrications and Applications of Boron Nitride Nanomaterials: A Review”. In: *Journal of Materials Science & Technology* 31.6 (2015), pp. 589–598.

[16] G.R. Bhimanapati, N.R. Glavin, and J.A. Robinson. “Chapter Three - 2D Boron Nitride: Synthesis and Applications”. In: *2D Materials*. Vol. 95. 2016, pp. 101–147.

[17] Francisco Guinea, MI Katsnelson, and AK Geim. “Energy gaps and a zero-field quantum Hall effect in graphene by strain engineering”. In: *Nature Physics* 6.1 (2010), p. 30.

[18] Ji Feng et al. “Strain-engineered artificial atom as a broad-spectrum solar energy funnel”. In: *Nature Photonics* 6.12 (2012), p. 866.

[19] Ivan Naumov, Alexander M Bratkovsky, and V Ranjan. “Unusual Flexoelectric Effect in Two-Dimensional Noncentrosymmetric s p 2-Bonded Crystals”. In: *Physical review letters* 102.21 (2009), p. 217601.

[20] Kuan Zhang and Marino Arroyo. “Understanding and strain-engineering wrinkle networks in supported graphene through simulations”. In: *Journal of the Mechanics and Physics of Solids* 72 (2014), pp. 61–74.

[21] Tao Jiang, Rui Huang, and Yong Zhu. "Interfacial sliding and buckling of monolayer graphene on a stretchable substrate". In: *Advanced Functional Materials* 24.3 (2014), pp. 396–402.

[22] K. Zhang and M. Arroyo. "Adhesion and friction control localized folding in supported graphene". In: *Journal of Applied Physics* 113.19 (2013), p. 193501.

[23] Sergei V. Kalinin and Vincent Meunier. "Electronic flexoelectricity in low-dimensional systems". In: *Phys. Rev. B* 77 (2008), p. 033403.

[24] S. M. Shandarov et al. "Detection of the contribution of the inverse flexoelectric effect to the photorefractive response in a bismuth titanium oxide single crystal". In: *JETP Letters* 95.12 (2012), pp. 618–621.

[25] Karel-Alexander N Duerloo, Mitchell T Ong, and Evan J Reed. "Intrinsic piezoelectricity in two-dimensional materials". In: *The Journal of Physical Chemistry Letters* 3.19 (2012), pp. 2871–2876.

[26] Karel-Alexander N. Duerloo and Evan J. Reed. "Flexural Electromechanical Coupling: A Nanoscale Emergent Property of Boron Nitride Bilayers". In: *Nano Letters* 13.4 (2013), pp. 1681–1686.

[27] HQgraphene. *Hexagonal Boron Nitrid (h-BN)*. http://www.hqgraphene.com/h-BN.php. Online; accessed 16 May 2018.

[28] Inc Engineering Department ULVAC-RIKO. *Model MILA-5000-UHV Infrared Lamp Heating system, Instruction Manual*. English. ULVAC-RIKO, Inc. 39 pp.

[29] Inc ADVANCE RIKO. *Mini Lamp Annealer MILA-5000 series*. https://advance-riko.com/en/products/mila-5000/. Online; accessed 21 May 2018.

[30] Nanosurf AG. *Operating principle of AFM*. https://www.nanosurf.com/en/how-afm-works/afm-operating-principle. Online; accessed 22 May 2018.

[31] Nader Jalili and Karthik Laxminarayana. "A review of atomic force microscopy imaging systems: application to molecular metrology and biological sciences". In: *Mechatronics* 14.8 (2004), pp. 907–945.

[32] Photonics media. *Dimension Icon, Bruker nanosurfaces*. https://www.photonics.com/pr62278/Dimension_Icon. Online; accessed 22 May 2018.

[33] Franz J Giessibl. "Advances in atomic force microscopy". In: *Reviews of modern physics* 75.3 (2003), p. 949.

[34] E Ukraintsev et al. "Artifacts in atomic force microscopy of biological samples". In: *Atomic Force Microscopy Investigations into Biology-From Cell to Protein*. InTech, 2012.

[35] Yong Chen. "Elucidation and identification of double-tip effects in atomic force microscopy studies of biological structures". In: *Journal of Surface Engineered Materials and Advanced Technology* 2.03 (2012), p. 238.

[36] Peter Eaton. *AFM Artifacts*. http://afmhelp.com/index.php?option=com_content&view=article&id=65:convolution. Online; accessed 29 May 2018.

[37] Ricardo Garcia and Alvaro San Paulo. "Attractive and repulsive tip-sample interaction regimes in tapping-mode atomic force microscopy". In: *Physical Review B* 60.7 (1999), p. 4961.

[38] F. Marchi et al. "Characterisation of trapped electric charge carriers behaviour at nanometer scale by electrostatic force microscopy". In: *Journal of Electrostatics* 66.9 (2008), pp. 538–547.

[39] Thierry Mélin, Mariusz Zdrojek, and David Brunel. "Electrostatic force microscopy and Kelvin force microscopy as a probe of the electrostatic and electronic properties of carbon nanotubes". In: *Scanning probe microscopy in nanoscience and nanotechnology*. Springer, 2010, pp. 89–128.

[40] NANOSENSOR. *PPP-NCHR*. http://www.nanosensors.com/PointProbe-Plus-Non-Contact-Tapping-Mode-High-Resonance-Frequency-Reflex-Coating-afm-tip-PPP-NCHR. Online; accessed 22 May 2018.

[41] Nysten B. “Electrostatic force microscopy and Kelvin probe force microscopy”. Unpublished Manuscript. 2018.

[42] S. Hudlet et al. “Evaluation of the capacitive force between an atomic force microscopy tip and a metallic surface”. In: *The European Physical Journal B - Condensed Matter and Complex Systems* 2.1 (1998), pp. 5–10.

[43] NANOSENSOR. *PPP-EFM*. http://www.nanosensors.com/PointProbe-Plus-Electrostatic-Force-Microscopy-PtIr5-Coating-afm-tip-PPP-EFM. Online; accessed 24 May 2018.

[44] Petr Klapetek, David Necas, and Christopher Anderson. *Artefacts de Convolution de Sonde*. http://gwyddion.net/documentation/user-guide-fr/tip-convolution-artefacts.html#tip-operations. Online; accessed 29 May 2018.

Rue Archimède, 1 bte L6.11.01, 1348 Louvain-la-Neuve **www.uclouvain.be/epl**